

# LONG-TERM EVOLUTION OF MASSIVE BLACK HOLE BINARIES. IV. MERGERS OF GALAXIES WITH COLLISIONALLY RELAXED NUCLEI

ALESSIA GUALANDRIS<sup>1</sup> AND DAVID MERRITT<sup>2</sup>

*Draft version November 8, 2018*

## ABSTRACT

We simulate mergers between galaxies containing collisionally-relaxed nuclei around massive black holes (MBHs). Our galaxies contain four mass groups, representative of old stellar populations; a primary goal is to understand the distribution of stellar-mass black holes (BHs) after the merger. Mergers are followed using direct-summation  $N$ -body simulations, assuming a mass ratio of 1:3 and two different orbits. Evolution of the binary MBH is followed until its separation has shrunk by a factor of 20 below the hard-binary separation. During the galaxy merger, large cores are carved out in the stellar distribution, with radii several times the influence radius of the massive binary. Much of the pre-existing mass segregation is erased during this phase. We follow the evolution of the merged galaxies for approximately three, central relaxation times after coalescence of the massive binary; both standard, and top-heavy, mass functions are considered. The cores that were formed in the stellar distribution persist, and the distribution of the stellar-mass black holes evolves against this essentially fixed background. Even after one central relaxation time, these models look very different from the relaxed, multi-mass models that are often assumed to describe the distribution of stars and stellar remnants near a massive BH. While the stellar BHs do form a cusp on roughly a relaxation time-scale, the BH density can be much smaller than in those models. We discuss the implications of our results for the EMRI problem and for the existence of Bahcall-Wolf cusps.

*Subject headings:* Galaxy:center - stellar dynamics

## 1. INTRODUCTION

The massive black holes (MBHs) that reside at the centers of some nearby galaxies are believed to grow together with their hosts through mergers: MBHs grow partly as a result of gas accretion, and partly by coalescence with other MBHs that are brought into the nucleus during the merger process (Begelman et al. 1980). The detailed assembly history of MBHs is poorly understood; major uncertainties include the “seed” mass distribution of MBHs at high redshift, the typical gas accretion efficiency, and the frequency with which MBHs are ejected due to gravitational-wave recoil (Kauffmann & Haehnelt 2000; Volonteri et al. 2003). But a robust prediction of the hierarchical models is that galaxies hosting MBHs in the nearby universe were formed from less massive systems, at least some of which already contained MBHs.

Binary MBHs created during galaxy mergers leave imprints on the stellar distribution: for instance, they create low-density cores, by exchanging energy with passing stars (Begelman et al. 1980; Milosavljević & Merritt 2001). Such cores are observed to be ubiquitous in stellar spheroids brighter than  $\sim 10^{10} L_{\odot}$  (Ferrarese et al. 1994; Lauer et al. 1995) and their sizes – of order the influence radius of the (presumably single) MBH – are consistent with the predictions of merger models (Graham 2004; Merritt 2006). Here we define the influence radius as

$$r_{\text{h}} \equiv \frac{GM_{\bullet}}{\sigma^2} \quad (1)$$

alessia@mpa-garching.mpg.de

<sup>1</sup>Max-Planck Institut für Astrophysik, Karl-Schwarzschild-Str. 1, D-85748 Garching, Germany

<sup>2</sup>Department of Physics and Center for Computational Relativity and Gravitation, Rochester Institute of Technology, 54 Lomb Memorial Drive, Rochester, NY

where  $\sigma$  is the rms velocity of stars in any direction at  $r \gtrsim r_{\text{h}}$ . Cores of radius  $\sim r_{\text{h}}$  become difficult to resolve in galaxies beyond the Local Group if the MBH mass is below  $\sim 10^8 M_{\odot}$ . Even in the nearest nucleus, that of the Milky Way, the presence of a parsec-scale core around Sgr A\* was only clearly established in the last few years (Buchholz et al. 2009).

In the absence of MBHs, mergers tend to preserve the form of the stellar distribution near the centers of galaxies (Dehnen 2005). Binary MBHs, however, are efficient at erasing the structure that was present on scales  $\lesssim r_{\text{h}}$  (Merritt & Cruz 2001), and this fact precludes drawing definite conclusions about the nuclear properties of the galaxies that preceded the hosts of observed MBHs. On the other hand, it is well established that low-luminosity galaxies have higher central densities than high-luminosity galaxies (Kormendy 1985). This is true both in terms of the mean density within the half-mass radius, and also in terms of the density on the smallest resolvable scales: low-luminosity spheroids often contain dense, nuclear stars clusters (NSCs), with sizes of order 10 pc and masses  $\lesssim 1\%$  the mass of the galaxy (Boeker 2010). NSC masses are therefore comparable to, or somewhat greater than, MBH masses (Ferrarese et al. 2006a), although NSCs have been shown to coexist with MBHs in only a handful of galaxies (Seth et al. 2008; Graham & Spitler 2009). The NSC in the Milky Way is believed to be a representative example: its half-light radius is 3 – 5 pc, or  $1 - 2r_{\text{h}}$ , and its mass is a few times  $10^7 M_{\odot}$ , or several times  $M_{\bullet}$  (Graham & Spitler 2009; Schödel 2011).

In the NSC of the Milky Way, the two-body relaxation time is comparable with the age of the universe, and this is consistent with the persistence of a core (as op-

posed to a Bahcall & Wolf (1976) cusp) in the late-type stars (Merritt 2010). But in fainter systems, central relaxation times are shorter. For instance, in the Virgo cluster, galaxies with NSCs have nuclear half-light relaxation times that scale with host-galaxy luminosity as (Merritt 2009)

$$T_{r,\text{NSC}} \approx 1.2 \times 10^{10} \text{yr} \left( \frac{L_{\text{gal}}}{10^{10} L_{\odot}} \right). \quad (2)$$

By comparison, the mean time between “major mergers” (mergers with mass ratios 3 : 1 or less) of dark-matter haloes in the hierarchical models varies from  $\sim 0.2$  Gyr at redshift  $z = 10$  to  $\sim 10^{10}$  yr at  $z = 1$ , with a weak dependence on halo mass (Fakhouri et al. 2010). This comparison suggests that the progenitors of many spheroids in the current universe may have been galaxies containing nuclei that were able to attain a collisionally-relaxed state before the merger that formed them took place.

In the absence of a MBH, collisional relaxation implies mass segregation and core collapse. If a MBH is present, mass segregation still occurs, but core collapse is inhibited by the fixed potential due to the MBH. A collisional steady state, which is reached by a time  $\sim T_r(r_h)$  at radii  $r \lesssim r_h$ , is characterized by a Bahcall-Wolf,  $n \sim r^{-7/4}$  cusp in the dominant component at  $r \lesssim 0.2r_h$ . If there is a mass spectrum, less-massive objects follow a shallower profile,  $n \sim r^{-3/2}$ , while more-massive objects follow a steeper profile,  $n \sim r^{-2}$  (Bahcall & Wolf 1977; Hopman & Alexander 2006).

As a first approximation, the mass spectrum of an evolved stellar population can be represented in terms of just two components: objects of roughly one solar mass or less (main-sequence stars, white dwarfs, neutron stars); and remnant black holes (BHs) with masses  $10 - 20 M_{\odot}$ . Standard initial mass functions predict that roughly 1% of the total mass will be in stellar BHs (Alexander 2005); so-called “top-heavy” mass functions (e.g. Bartko et al. 2010) predict a larger fraction. In a collisionally relaxed nucleus, the density of stellar BHs will rise more steeply toward the center than the density of the stars. Mergers between galaxies with such nuclei would be expected to modify these steady-state distributions substantially, and also to affect (increase) the time scale over which a collisionally relaxed cusp could be re-generated following the merger (Merritt & Szell 2006).

These arguments motivated us to carry out merger simulations between galaxies containing multi-component, mass-segregated nuclei around MBHs. As in previous papers from this series (Milosavljević & Merritt 2001; Berczik et al. 2005; Merritt et al. 2007b), our merger simulations are purely stellar-dynamical. In some galaxies, torques from gas would assist in the evolution of binary MBHs (Escala et al. 2005; Dotoli et al. 2007; Cuadra et al. 2009). Gas also implies star formation, and there is evidence for complex star formation histories in many NSCs (Walcher et al. 2006). But  $N$ -body simulations that allow for non-spherical geometries (Berczik et al. 2006; Khan et al. 2011) have shown that purely dissipationless energy exchange with ambient stars can bring binary MBHs to milliparsec separations on time scales much shorter than galaxy lifetimes. Unless the late evolution of the binary MBH is greatly accelerated by torques from the gas, the influence of the bi-

nary on the distribution of the *stellar* populations should be accurately reproduced by our dissipationless models. With respect to star formation, population synthesis of NSC spectra suggest that most of the mass typically resides in stars with ages of order 5-10 Gyr (Figer et al. 2004; Boeker 2010), i.e. an old population.

Simulating the merger of galaxy-sized systems, while enforcing the spatial and temporal resolution required to faithfully reproduce the dynamics of stars on scales  $\ll r_h$  around the central MBH, is computationally demanding. Our simulations used  $\sim 10^6$  particles per galaxy, and the models were advanced using a parallel, direct-summation  $N$ -body code (Harfst et al. 2007). The integrations were accelerated using special-purpose hardware. The galaxy models contained four mass groups, representing an evolved stellar population. Initial conditions of the merging galaxies were constructed in a two-stage process: models of mass-segregated nuclei around a MBH were first constructed, then these collisionally-relaxed models were imbedded into larger, spheroid-sized models. Mergers were then carried out, assuming a galaxy mass ratio of 1 : 3.

A major motivation for our new simulations was the need to understand the distribution of stellar remnants, particularly stellar-mass BHs, near the centers of galaxies. Knowledge of the BH density well inside  $r_h$  is crucial for predicting the rates of many astrophysically interesting processes; in particular, the rate of capture of stellar-mass BHs by MBHs, or EMRIs (Amaro-Seoane et al. 2007). Published EMRI rate calculations almost always assume a state of mass segregation, implying a high density of stellar remnants near the MBH (Hopman & Alexander 2006; Hopman 2009). However, in a nucleus formed via a merger, any pre-existing mass segregation would have been disrupted by the binary MBH when it created a core; whether or not the massive remnants would have had time to re-segregate following the merger is difficult to assess without full  $N$ -body simulations.

Our simulations followed the evolution of the binary MBHs for a time almost long enough that gravitational wave emission would dominate the binaries’ evolution. We then combined the two MBH particles into one, simulating gravitational wave coalescence, and continued the  $N$ -body integrations for a time corresponding to several relaxation times at the (new) influence radius. In this post-merger evolutionary phase, we also considered the consequences of varying the relative numbers of the different mass components. In this way, we were able, for the first time, to observe how rapidly the stellar BHs would re-segregate following a merger. We found substantially longer time scales for this evolution than in earlier simulations that started from physically less motivated initial conditions.

The paper is organized as follows. In Section 2 we describe the procedure to generate equilibrium segregated models starting from single-component models. Scaling to physical units is discussed in Section 3. Evolution of the binary MBH and its effects on the underlying stellar distribution are described in Section 4. In Section 5 we describe the evolution of the light and heavy objects after the massive binary has undergone coalescence. Section 6 describes the shapes and kinematics of the merger remnants. Section 7 discusses the implications of our re-

sults for the formation and observability of Bahcall-Wolf cusps, and for the distribution of stellar remnants.

## 2. INITIAL MODELS AND NUMERICAL METHODS

Multi-mass Fokker-Planck models have been constructed for stars around a MBH (e.g. Hopman & Alexander 2006). Extending these models beyond  $r_h$  – where the stellar distributions are expected to be unrelaxed and where the gravitational potential contains contributions from stars as well as from the MBH – is problematic. Instead, we used  $N$ -body integrations to create models of galaxies with collisionally-relaxed nuclei. The major difficulty was obtaining sufficient resolution on the scale of the relaxed density cusp, without using a prohibitively large number of particles overall. In brief, we proceeded as follows.

1. A mass-segregated model of the inner parts of a galaxy containing a MBH was created via  $N$ -body integrations, starting from a configuration in which the different mass groups all had the same phase-space distribution. This model had a total mass of  $50M_\bullet$ ; scaled to a galaxy like the Milky Way, the outer radius of the model would be  $\sim 10$  pc.

2. Smooth representations of the density profiles were constructed for each of the  $N$ -body species at the end of the integration. These functions were then “spliced” onto a larger, unrelaxed model, at a radius where the effects of mass segregation were essentially zero. This larger model had a mass of  $200M_\bullet$ , or roughly  $1/5$  the mass of an entire stellar spheroid.

3. The smooth functions representing the different mass components in this larger model were used to generate Monte-Carlo positions and velocities as initial conditions for the  $N$ -body integrations.

4. Two such  $N$ -body models, with different total masses and radii, were placed in orbit around each other and integrated forward until the two MBH particles had formed a tightly-bound pair at the center. At this time, the merged galaxy contained a large, low-density core created by the binary MBH.

5. The two MBH particles were combined into a single particle and the merged galaxy was re-sampled using a smaller  $N$ . This model was then integrated forward for a few central relaxation times, allowing the different mass groups to again evolve toward a collisional steady state near the center.

In more detail, the mass-segregated models described in step 1 were created as follows.

Initial conditions were generated from a density law having roughly the expected, steady-state distribution near the MBH. We used the modified Prugniel-Simien (1997) model described by Terzić & Graham (2005), which has a central density cusp of adjustable slope:

$$\rho(r) = \rho' \left[ 1 + \left( \frac{r_s}{r} \right)^\alpha \right]^{\gamma/\alpha} \left[ (r^\alpha + r_s^\alpha) / r_{\text{PS}}^\alpha \right]^{-p/\alpha} \times \exp \left\{ -b \left[ (r^\alpha + r_s^\alpha) / r_{\text{PS}}^\alpha \right]^{1/n\alpha} \right\}. \quad (3)$$

Setting  $\gamma = 3/2$  in the first term gives  $\rho \sim r^{-3/2}$  near the center, which is close to the collisionally-relaxed density profile expected for the dominant population in a multi-mass cusp (e.g. Hopman & Alexander 2006). The parameter  $r_s$  determines the extent of the cusp;

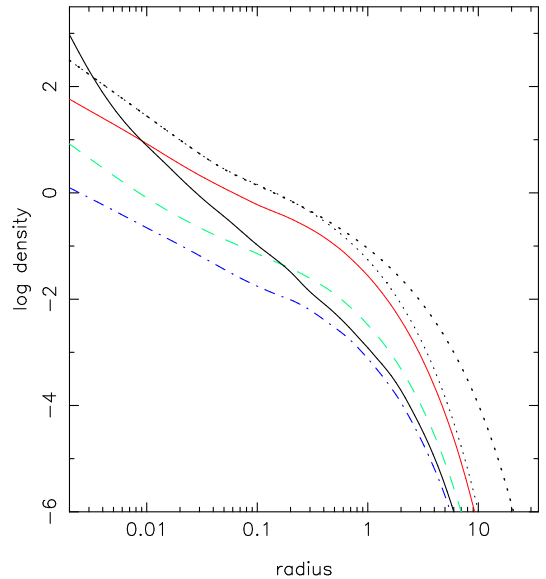


FIG. 1.— Thin, dotted (black) curve is the density profile of the initial, non-mass-segregated model, equation (3). Other curves show mass density profiles of the four species after integration for  $\sim 1.5$  central relaxation times:  $1M_\odot$  main-sequence stars (thin, red);  $0.6M_\odot$  white dwarfs (dashed, green);  $1.6M_\odot$  neutron stars (dash-dotted, blue) and  $10M_\odot$  stellar black holes (thick, black). Each curve represents the combined density of eight independent integrations with 132k particles. Scaled to the Milky Way, the unit of length is approximately 10 pc and the total mass is approximately  $2 \times 10^8 M_\odot$ . Thick dotted (black) curve shows the second, more extended analytical model into which the mass-segregated cusp was imbedded; this model has four times the mass of the first model.

in relaxed, single-component models,  $r_s \approx 0.2r_h$  (e.g. Merritt & Szell 2006). The parameter  $p$  sets the power-law slope beyond the central cusp; we set  $p = 0.5$ , i.e. a relatively constant density like that of the nuclear stellar disk of the Milky Way. The two final terms on the right hand side of equation (3) mimic a deprojected Sérsic-law galaxy, with  $n$  the Sérsic index; the parameter  $b$  can be related to  $n$  if  $r_{\text{PS}}$  is identified with the effective radius (Terzić & Graham 2005). In our case, the exponential term is invoked only to provide a sharp truncation to the model outside of  $\sim$  a few  $r_h$ ; we set  $n = 1.5$ . Given these parameters, and setting  $\alpha = 4$ , we could then solve for the cusp radius  $r_s$  in units of the model scale-length  $r_{\text{PS}}$ :  $r_s \approx 0.05r_{\text{PS}}$ . The result is shown as the thin dotted curve in Figure 1.

This initial model was assigned a mass of  $50M_\bullet$ . If we equate  $M_\bullet$  and  $r_h$  with their values in the Milky Way (respectively  $\sim 4 \times 10^6 M_\odot$  and  $\sim 2.5$  pc), the unit of length is  $\sim 10$  pc and the total mass is  $\sim 2 \times 10^8 M_\odot$ . Henceforth we refer to this subsystem as the NSC.

The NSC model was assumed to be made up of four discrete mass groups. The relative values of the particle masses were  $1 : 0.6 : 1.4 : 10$ . These represent, respectively, one-solar-mass main sequence stars (MS); white dwarfs (WD); neutron stars (NS); and  $10 M_\odot$  black holes (BH). The relative numbers of the four populations were set to

$$N_{\text{MS}} : N_{\text{WD}} : N_{\text{NS}} : N_{\text{BH}} = 1 : 0.2 : 0.02 : 0.005, \quad (4)$$

independent of radius. In reality, these fractions would depend on the initial mass function and the star forma-

tion history. Standard values are

$$N_{MS} : N_{WD} : N_{NS} : N_{BH} \approx 1 : 0.1 : 0.01 : 0.001 \quad (5)$$

(e.g. Alexander 2005). By comparison, our model contains roughly twice the numbers of WDs and NSs and five times the number of BHs. This was done in order to improve the statistics for the remnant populations, particularly the BHs. Our choices could also be seen as corresponding to a “top-heavy” initial mass function (e.g. Maness et al. 2007). In our post-merger simulations, we explored the consequences of varying these ratios.

Initial positions and velocities of particles from the four mass groups were generated in a standard way: (i) The gravitational potential  $\Phi(r)$  was computed from the known mass distribution (equation 3) plus the central MBH particle. (ii) The function  $N(< v, r)$ , the cumulative distribution of velocities at each radius, was computed as in Szell et al. (2005) from  $\rho(r)$  and  $\Phi(r)$ , assuming an isotropic velocity distribution. (iii) Monte-Carlo positions and velocities were generated from  $N(< v, r)$  for each of the four mass groups, with the relative numbers given by equation 4.

We generated eight such models, each containing 131071 particles, using different initial seeds for the random number generator in each case. We then independently integrated these eight models forward for a time corresponding to roughly 1.5 central relaxation times as defined by equation (7) (using for  $m$  the mass of a MS particle). The initial relaxation time (which is independent of radius near the MBH in a  $\rho \sim r^{-3/2}$  cusp) was roughly 130 in model units ( $G = M = r_{PS} = 1$ ). We used the direct-summation  $N$ -body code  $\phi$ GRAPE (Harfst et al. 2007), integrating each model on one node of the RIT GRAPE cluster. Figure 2 shows the evolution of the Lagrange radii for the four mass groups. This figure combines data from the eight independent  $N$ -body integrations; the total number of particles represented is roughly one million. The stellar BHs (of total number  $8 \times 635 = 5080$ ) accumulate toward the center; by  $t = 200$ , their distribution appears to have reached a steady state inside  $\sim 0.1 \approx 1$  pc. The lighter populations evolve less, as expected, since their distribution was close to the steady-state form at the start (by design). The final density profiles of the four populations are shown in Figure 1. The BHs follow  $\rho \sim r^{-2}$  at  $r \lesssim 0.1 \approx 1$  pc, and they dominate the total (mass) density inside  $r \approx 0.007 \approx 0.07$  pc. The density cusp defined by the less massive populations is nearly unchanged aside from a slight expansion due to heating by the BHs.

The mass-segregated model was then imbedded into a more extended, unsegregated model with four times the total mass. The template for this larger model is shown as the thick dotted line in Figure 1. It follows the same density law as in equation (3), but with larger scale length  $r'_{PS}$ . The imbedding was achieved as follows: Smoothed density profiles were constructed from each of the four mass groups in the evolved  $N$ -body model (the same functions plotted in Figure 1). These smooth profiles were then matched onto the density of the extended model at a radius  $\sim 0.3r_{PS}$ ; beyond this radius, essentially no evolution occurred in the  $N$ -body integrations and so the  $N$ -body density profiles (with appropriate vertical scalings) matched well onto the analytic profile.

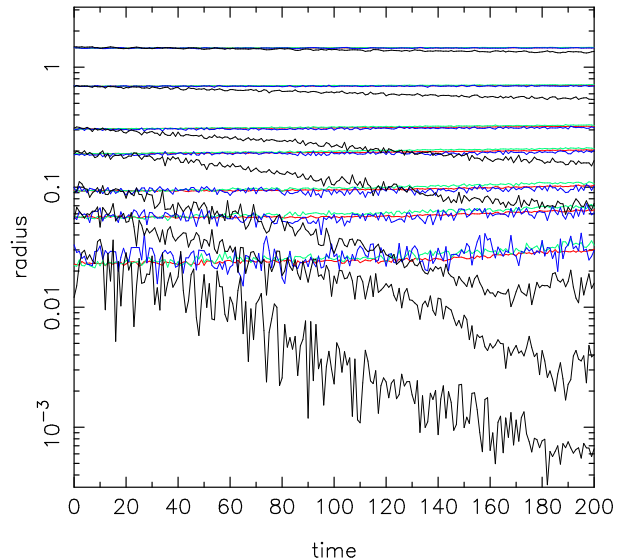


FIG. 2.— Lagrange radii of the four stellar species during the  $N$ -body integrations of the initial model shown in Figure 1. This plot is based on the roughly one million particles in the 8, independent integrations of that model generated with different random number seeds. *Red*:  $1 M_{\odot}$  main-sequence stars; *green*:  $0.6 M_{\odot}$  white dwarfs; *blue*:  $1.6 M_{\odot}$  neutron stars; *black*:  $10 M_{\odot}$  stellar BHs. The BHs form a dense cluster around the MBH in approximately one, central relaxation time as defined by the main-sequence stars. The lighter populations are pushed slightly outward during this time. Scaled to the Milky Way, the approximate unit of length is 10 pc.

A small degree of smoothing was nevertheless necessary near the matching radius to keep the first derivatives of the density continuous. Finally, small (a few percent) adjustments were made in the vertical normalizations of the four density profiles in order to recover precisely the original ratios between the total numbers of the four species.

The total mass of this extended model was 200 times the MBH mass. Since observed bulge masses are  $\sim 10^3 M_{\bullet}$ , such a model can be interpreted as comprising the innermost  $\sim 20\%$  of a real bulge. In what follows, we refer to this model as “the bulge.”

$N$ -body realizations of the bulge models were then constructed in the same way as described above. Two such models were required for each merger simulation. We considered unequal-mass mergers with a mass ratio of 3 : 1. The radius of the smaller bulge was scaled as the square-root of the bulge mass. Particle masses (aside from the MBH particle) were the same in the two bulges, i.e., particle number scaled linearly with total mass.

Table 1 lists the important parameters of the merging systems: the mass ratio of the two MBHs (equal to the galaxy mass ratio), the ratio of MBH mass to host bulge mass, the ratio of the MS stars mass to MBH mass, the number of particles in each galaxy, and the initial separation between the bulge centers,  $\Delta r$ , expressed in units of the outer radius of the larger bulge,  $R_1$ . The table also gives the influence radius associated with the MBH in the larger galaxy, under two definitions. In addition to the first definition given in equation 1, we also compute a second, mass-based influence radius: the radius  $r_m$  that contains a mass in stars equal to twice the MBH mass:

$$M_{\star}(r < r_m) = 2M_{\bullet}. \quad (6)$$

The mass-based definition is the most straightforward to

TABLE 1  
GALAXY MERGER PARAMETERS

$M_1 : M_2$	$M_\bullet / M_{\text{gal}}$	$M_{\text{MS}}/M_\bullet$	$N_1$	$N_2$	$\Delta r/R_1$	$r_h$	$r_m$
3:1	0.005	0.0005	400k	120k	1.5	0.10	0.28

TABLE 2  
POST-MERGER MODELS

Model	$N$	Fractions	$M_\bullet/M_{\text{gal}}$
A1	250k	1:0.2:0.02:0.005	0.0050
A2	225k	1:0.1:0.01:0.001	0.0055
B1	250k	1:0.2:0.02:0.005	0.0050
B2	225k	1:0.1:0.01:0.001	0.0055

apply in  $N$ -body models like ours; in computing  $r_h$ , a choice must be made about the radius at which to evaluate  $\sigma$ , and this, combined with the need to bin particles, can lead to factor of  $\sim$  two uncertainties in  $r_h$ . The values of  $r_h$  and  $r_m$  in Table 1 refer to the larger of the two galaxies.

The two bulge models were placed far enough apart initially that there was no overlap, but not much farther, in order to minimize the integration time. Two relative orbits were considered: a circular orbit (Model A), and an eccentric orbit in which the initial relative velocity was set to 0.7 times the circular value (Model B).

The merger simulations were also carried out using  $\phi$ GRAPE, both in combination with GRAPE hardware at the Rochester Institute of Technology and with GPU hardware at the Max-Planck Institute for Astrophysics in Garching by means of the Sapporo library (Gaburov et al. 2009). We conservatively set the accuracy parameter (Harfst et al. 2007) to 0.005 and the softening to  $10^{-4}$  (in  $N$ -body units). Such small values of the softening and accuracy parameters were necessary to accurately follow the dynamics of the massive binary.

The simulations were continued until the two MBH particles had formed a tight binary and the binary separation had shrunk by an additional factor of  $\sim$  20. At this time, the two MBH particles were combined into a single particle, which was placed at the center-of-mass position and velocity of the binary. A random subset of particles was then chosen from this model, yielding a new model with the same phase-space distributions of the four components but a smaller total  $N$ . This ‘‘merged galaxy’’ model was then integrated forward, for a time corresponding to a few central relaxation times. The subsampling was a necessary compromise to keep the physical integration time from becoming prohibitively long while still allowing the simulations to proceed for more than one relaxation time. For each of the models presented in Table 1 we generated two different submodels with different number fractions, as illustrated in Table 2. In order to generate the models with the standard fractions  $N_{\text{MS}} : N_{\text{WD}} : N_{\text{NS}} : N_{\text{BH}} \approx 1 : 0.1 : 0.01 : 0.001$ , we deleted an appropriate number of particles in each mass group from the models with  $N_{\text{MS}} : N_{\text{WD}} : N_{\text{NS}} : N_{\text{BH}} = 1 : 0.2 : 0.02 : 0.005$ .

### 3. SCALING

In any  $N$ -body simulation, an important consideration is how to relate the computational units of mass, length and time to physical units. In our simulations, the mass scale is most naturally set by the mass of the particle(s) representing the MBH(s), and the length scale by the radius that encloses a mass in stars that is some multiple of the MBH mass. A natural choice for the latter is  $r_m$ , as defined in equation (6). Identifying  $r_m$  in the simulations with  $r_m$  in a real galaxy is only justified, of course, to the extent that the radial dependence of the density near the MBH is similar in both systems.

Scaling of the time is more subtle. Two basic time scales are of interest: the crossing time, which is determined by the total mass and size of the model; and the relaxation time, which depends as well on the masses of the particles, or equivalently on  $N$ :

$$T_r = \frac{0.33 \sigma^3}{G^2 n m^2 \ln \Lambda} \quad (7)$$

(Spitzer 1987). Here,  $n$  is the stellar number density,  $m$  is the mass of one star, and  $\ln \Lambda$  is the Coulomb logarithm. The particle masses in our simulations have the correct ratios with respect to one another, but their masses in relation to the total galaxy mass is much larger than in a real galaxy – due of course to the fact that our  $N$  is much smaller than  $10^{11}$ . While there is a well-defined relaxation time in the models, that time is much shorter relative to the crossing time than it would be in real galaxies.

These statements apply to many  $N$ -body simulations that extend over relaxation time scales. A novel feature in our simulations is the treatment of the galaxy merger. Such a merger requires of order a few crossing times in order to reach a (collisionless) steady state. Since crossing times are much shorter than relaxation times, both in reality and in our models, a galaxy would not undergo a significant amount of collisional relaxation during the merger. During this phase of the simulations, therefore, the appropriate unit of time is the crossing time. In the phases preceding and following the merger, the appropriate unit of time is the relaxation time.

Subtleties arise when one considers the massive binary. After the galaxy merger is essentially complete, the binary MBH continues to evolve. In a spherical nucleus, the binary quickly ejects stars on intersecting orbits, and continued hardening takes place on a relaxation time scale, as stars are scattered by other stars onto previously-depleted orbits that intersect the binary (Makino & Funato 2004; Merritt et al. 2007b). In such models, there is effectively just one time scale – the relaxation time – that determines both the rate of collisional evolution of the galaxy and of the central binary following the merger.

Another mode of evolution is possible, if the galaxy potential is significantly nonspherical (Merritt & Poon 2004; Berczik et al. 2006). In this case, orbital angular momenta of stars near the massive binary evolve due both to encounters, and to torques from the overall stellar potential. Typically the latter dominates, and the supply of stars to the massive binary remains high in spite of ongoing, slingshot ejections. The binary evolves at a rate that is fixed essentially by stellar orbital periods, i.e. by the crossing time, and not by the relaxation time. Such

evolution appears to be the norm when the galaxy hosting the massive binary was formed in a realistic merger simulation (Khan et al. 2011; Preto et al. 2011), and we find the same result in our new simulations. This result simplifies the time scaling of our models, since it means that a single physical time – the crossing time – sets the rate of evolution, both during the galaxy merger, and immediately afterwards, as the massive binary hardens.

One potential difficulty does arise, however. If hardening of the massive binary is simulated for a time that is comparable with the  $N$ -body central relaxation time, some collisional evolution in the stellar distribution will occur. This may or may not be realistic, since in a real galaxy, the ratio of relaxation time to crossing time is much larger than in the simulations. For this reason, the models that we adopt at the start of the final phase of our simulations – single galaxies containing merged MBHs – may exhibit overly-segregated nuclei, causing the subsequent, collisional relaxation to occur more quickly than it would in a real galaxy.

#### 4. THE GALAXY MERGER

##### 4.1. Evolution of the massive binary

Figures 3 and 4 illustrate the large-scale evolution of the bulge models described in Table 1 during the galaxy merger phase. The two bulge models start out either on circular (Model A) or eccentric (Model B) orbits about their common center of mass, with initial separations roughly one-half the radius of the larger bulge. Due to its more eccentric initial orbit, Model B evolves more quickly. The trajectories of the MBHs reflect the initial orbits of the parent systems, as can be seen in Figure 5.

Evolution of a binary MBH can be divided roughly into four phases. (1) *Formation of a bound pair*. Merger of two galaxies with central MBHs brings the two MBHs together, in a time comparable with the galaxy merger time, i.e. a few galaxy crossing times. (2) *Formation of a hard binary*. The separation between the two MBHs decreases very rapidly, due at first to dynamical friction against the stars, and then to the gravitational slingshot: near stars are ejected after gaining energy from the massive binary. A core is formed at this stage, with size roughly equal to the initial separation of the bound pair. (3) *Binary hardening*. If orbits of stars ejected by the gravitational slingshot are replenished, the massive binary will continue to shrink. Hyper-velocity stars can be produced in this process. The stellar core will continue to grow. (4) *Coalescence*. If replenishment of stellar orbits continues, the binary separation decreases to a value such that emission of gravitational waves dominates its evolution, and the two MBHs coalesce.

Dynamical friction drives the evolution down to a separation  $a_f$  at which the stellar mass enclosed in the binary is of order twice the mass of the smaller MBH:

$$M(< a_f) \approx 2 M_2. \quad (8)$$

This separation is smaller by a factor  $\sim M_2/M_1$  than the radius of influence of the larger MBH.

At separations smaller than  $a_f$ , the binary hardens due to gravitational slingshot interactions with passing stars. A binary is defined as “hard” when it reaches a separation

$$a_h \approx \frac{G M_2}{4 \sigma^2} \quad (9)$$

called the hard-binary separation; a binary is “hard” when its binding energy per unit mass,  $|E|/(M_1 + M_2)$ , exceeds  $\sigma^2$ .

The binary enters the gravitational wave (GW) regime when the time scale for coalescence due to emission of gravity waves:

$$\begin{aligned} T_{\text{GW}} &= \frac{5}{256 F(e)} \frac{c^5}{G^3} \frac{a^4}{\mu (M_1 + M_2)^2} \\ &\approx \frac{5.8 \times 10^{11} \text{ yr}}{F(e)} \left( \frac{a}{0.1 \text{ pc}} \right)^4 \left( \frac{10^7 M_\odot}{\mu} \right) \left( \frac{10^8 M_\odot}{M_1 + M_2} \right)^2 \end{aligned} \quad (10)$$

becomes shorter than the time for hardening due to stellar interactions. Here

$$F(e) = (1 - e^2)^{-7/2} \left( 1 + \frac{73}{24} e^2 + \frac{37}{96} e^4 \right)$$

and  $\mu \equiv M_1 M_2 / (M_1 + M_2)$  is the reduced mass.

The evolution of the separation between the MBHs is shown in Figure 6. The first part of this evolution, which is driven by dynamical friction, ends when the separation reaches  $\sim a_f$ , equation (8);  $a_f \approx 0.9$  in model units. The time to reach this separation was  $t_f \approx 440$  and  $\sim 160$ , respectively, for models A and B. At about the same time, gravitational slingshot encounters with the stars begin to dominate the binaries’ evolution and the effect on the galaxy structure starts to become apparent. Figure 7 clearly shows a decrease in the central densities of both the main-sequence stars and the stellar BHs at a time  $t \approx t_f$ . Similar expansions are observed in the white dwarf and neutron star distributions. However, the stellar BHs are most affected, due to their higher, initial central concentration.

The orbital semi-major axis and eccentricity of the massive binary are shown as functions of time in Figure 8. Even in the circular-orbit merger (Model A), the massive binary forms with a slightly nonzero eccentricity. Subsequent evolution of  $a$  and  $e$  is driven by interactions with stars on intersecting orbits.

We computed the time-dependent binary hardening rate (Quinlan 1996)

$$s \equiv \frac{d}{dt} \left( \frac{1}{a} \right) \quad (11)$$

by fitting a straight line to  $a^{-1}(t)$  in small time intervals between the time of binary formation and the end of the integration. The results are shown in the bottom panels of Figure 9 for both models. The top panels show the evolution of  $1/a$ . The hardening rate appears roughly constant in time, which suggests that the binaries enter the hard phase rather quickly, and then continue hardening at an approximately constant rate. This behavior is a defining property of hard binaries, if the stellar background is unchanging, i.e. unaffected by the binary.

Mikkola & Valtonen (1992), Quinlan (1996) and Sesana et al. (2006) performed three-body scattering experiments of circular binaries of varying mass ratio and hardness to derive estimates of the hardening rate. They provided fitting formulae for the dimensionless param-

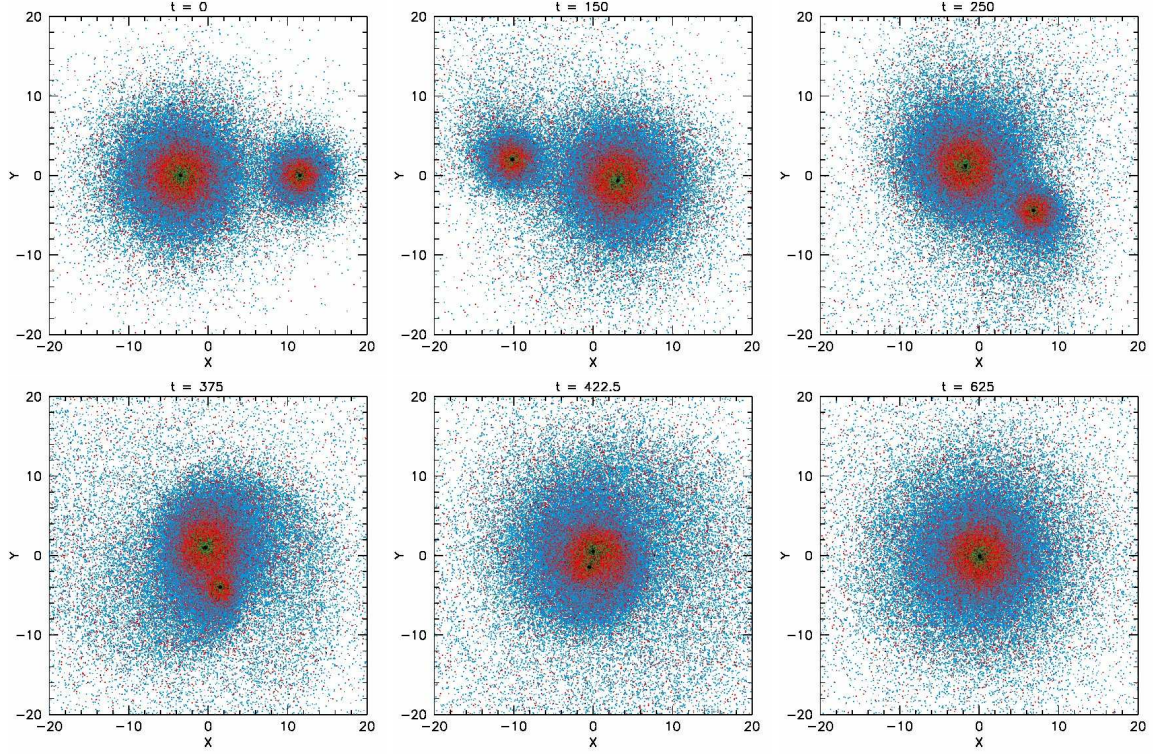


FIG. 3.— Snapshots from the early evolution of Model A. The different colors refer to the different mass groups: main sequence (blue), white dwarfs (red), neutron stars (green), black holes (black). The MBHs are indicated by full circles.

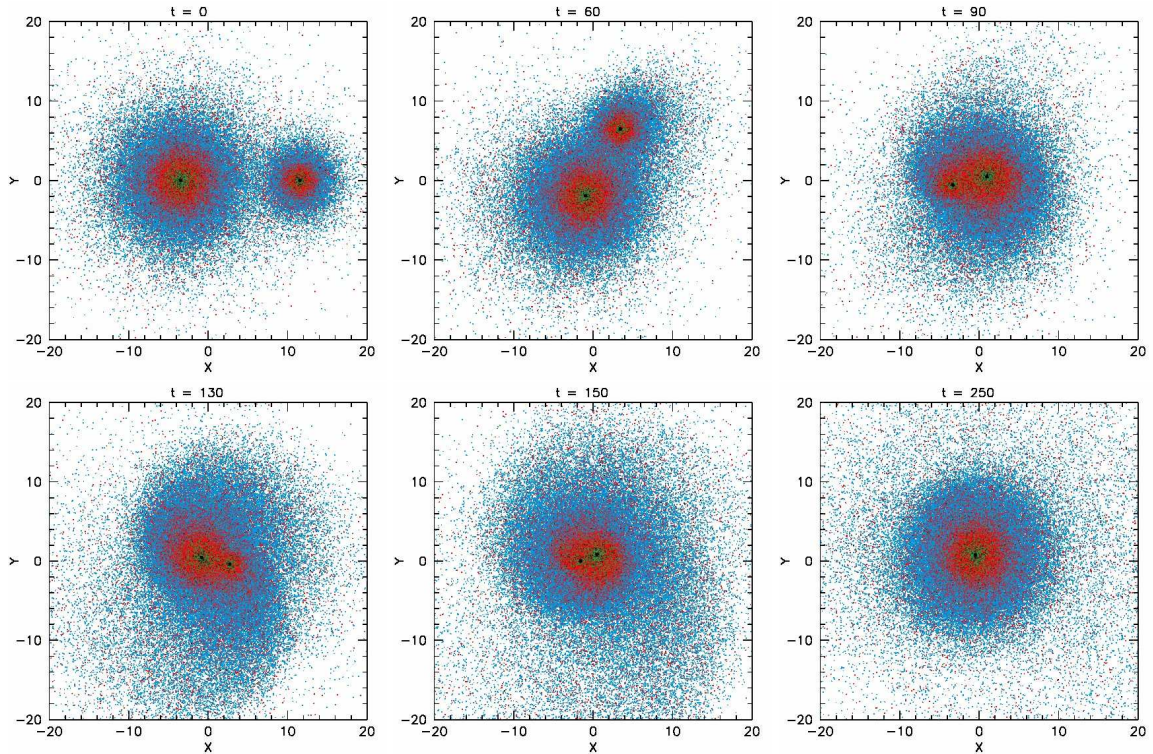


FIG. 4.— Snapshots from the early evolution of Model B. Colors are as in Figure 3.

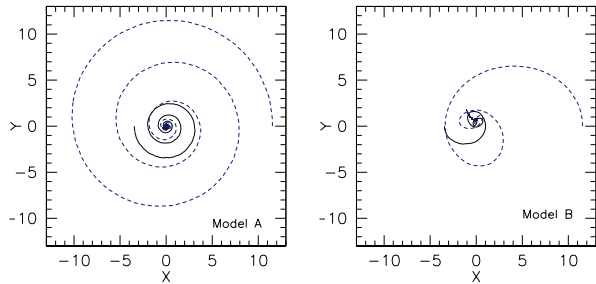


FIG. 5.— Trajectories of the MBHs in Model A (left) and B (right) during the galaxy merger phase. Dashed line: trajectory of the smaller hole. Solid line: trajectory of the larger hole. The initial orbit of the galaxy pair lies in the  $z = 0$  plane.

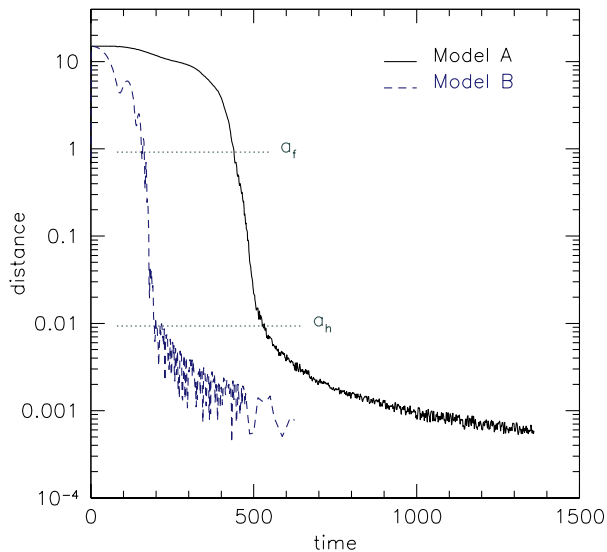


FIG. 6.— Separation between the MBH particles as a function of time. The horizontal lines indicate  $a_f$ , the approximate separation at which dynamical friction ceases to be efficient (equation 8), and  $a_h$ , the hard-binary separation (equation 9).

ter  $H$  which is related to the hardening rate via

$$H(a) = \frac{\sigma}{G\rho} \frac{d}{dt} \left( \frac{1}{a} \right), \quad (12)$$

where  $\rho$  is the stellar mass density and  $\sigma$  is the one-dimensional velocity dispersion, both assumed constant in space and time and unaffected by the presence of the binary. The  $H$  parameter obtained from these scattering experiments is a function of binary mass ratio and hardness; the latter is defined in terms of  $V_{\text{bin}}/\sigma$ , the ratio of binary circular speed to field-star velocity dispersion.

We wish to compare the  $N$ -body results for  $s$  with the predictions from the scattering experiments. Good agreement would imply a “full loss cone,” i.e. that the rate of interaction of the binary with stars is unaffected by slingshot ejections. In spherical galaxy models, binary hardening rates fall much below the predictions from the scattering experiments, since orbital repopulation is driven by two-body scattering, which is a slow process for large  $N$  (Makino & Funato 2004; Berczik et al. 2005;

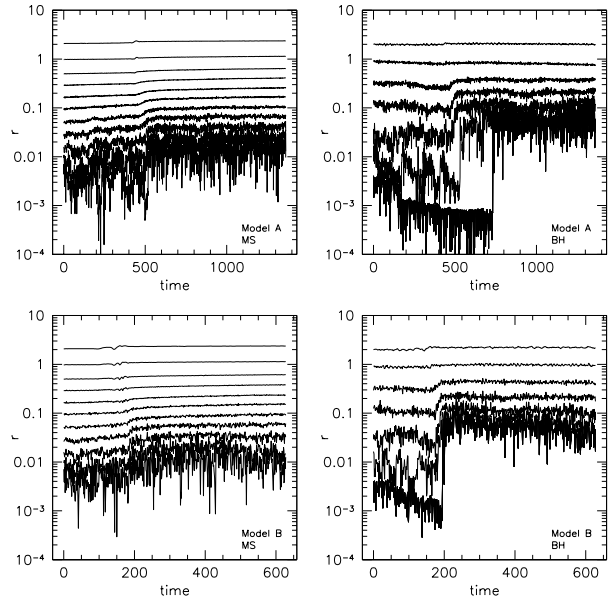


FIG. 7.— Evolution of the Lagrange radii of the main sequence stars (left) and stellar BHs (right) during the galaxy merger phase, for models A (top) and B (bottom). For clarity, only stars initially belonging to the larger galaxy are shown. Formation of the binary MBH is reflected in the sudden expansion of the central regions, at  $t \approx 500$  (Model A) and  $t \approx 200$  (Model B).

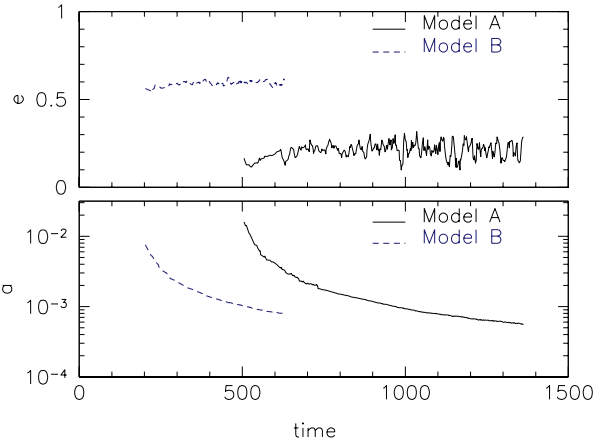


FIG. 8.— Evolution of the semi-major axis and eccentricity of the MBH binary in Model A and B, starting from the time when the MBHs are formally bound.

Merritt et al. 2007b).

We defined the theoretically-expected hardening rate to be

$$s_D(a) \equiv H(a) \left( \frac{\rho}{\sigma} \right)_D \quad (13)$$

where  $H$  is taken from the published scattering experiments, and  $\rho$  and  $\sigma$  are measured in our  $N$ -body models, at a distance  $D$  from the MBH. ( $G = 1$  in  $N$ -body units.) For  $H(a)$  we adopted the fitting formula of Sesana et al. (2006):

$$H = A(1 + a/a_0)^\gamma, \quad a_0 = 1.05 \frac{GM_2}{\sigma^2} \quad (14)$$

with parameters for a 3 : 1 mass ratio:  $A = 15.82$ ,  $\gamma =$



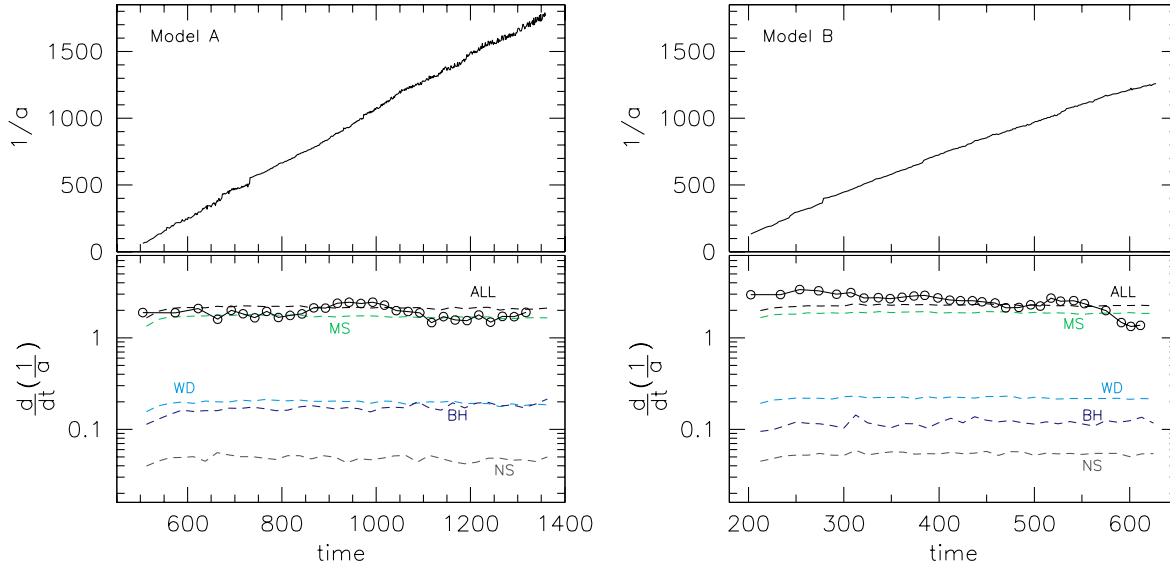


FIG. 9.— Evolution of the inverse binary semi-major axis (upper) and the binary hardening rate (lower). The points represent the  $N$ -body results while the dashed lines represent the semi-analytic estimates for the different mass groups, assuming a full loss cone regime and evaluating the density and velocity dispersion at  $D = 0.5$  from the binary center of mass.

$-0.95$ . Because  $\rho$  and  $\sigma$  vary with position (and time) in the  $N$ -body models, our computed values of  $s$  will depend on  $D$ . We found this dependence to be weak, as long as  $D$  is not too different (i.e. not more than a factor of two) from  $r_m$ : both  $\rho$  and  $\sigma$  are weakly dependent on radius for  $r \approx r_m$ . In Figure 9 we plot values of  $s_D$  for  $D = 0.5$ , slightly larger than estimated influence radii in both models. We find that the  $N$ -body hardening rates,  $s$ , are quite consistent with the analytic predictions  $s_D$ . The contributions to the binary hardening from the different mass groups (assumed to scale in proportion to their mass densities) are shown in the bottom panels of Figure 9. The MS stars appear to be responsible for most of the binary hardening, followed by the white dwarfs and the stellar black holes.

These results suggest that the massive binaries in our simulations are roughly in the “full-loss-cone” regime: they harden at a rate that is consistent with the expected hardening rate of a binary in an undepleted field of stars. This is in agreement with the results of Khan et al. (2011) and Preto et al. (2011), who also found that the stalling that occurs in spherical models is absent in simulations that start from a stage preceding merger of the two galaxies. Apparently, the non-spherical shapes of the merger remnants result in a large population of stars on “centrophilic” orbits: saucer orbits in the axisymmetric geometry (Sridhar & Touma 1999), pyramid orbits in the triaxial geometry (Merritt & Vasiliev 2010), etc. We discuss the shapes of our models in more detail in Section 6.

Figure 8 shows that the eccentricity of the massive binary remains roughly constant in both models. In a nonrotating galaxy, binary eccentricity is expected to increase gradually with time:

$$\frac{de}{dt} = K \frac{d \ln(1/a)}{dt} \quad (15)$$

where  $K > 0$  is a second dimensionless rate, also

derivable from scattering experiments; for instance, Sesana et al. (2006) give

$$K = A(1 + a/a_0)^\gamma + B, \quad (16)$$

and their Table 3 gives values of  $A$  and  $B$  for a 1 : 3 binary mass ratio. Stars that encounter the binary in a prograde (co-rotating) sense tend to circularize it; Sesana et al. (2011) found that when the fraction of corotating stars exceeded  $\sim 0.7$  (as opposed to 0.5 for a nonrotating galaxy), binaries tend to circularize. We found that our models have roughly this fraction ( $\sim 0.7$ ) of corotating stars, consistent with the mild eccentricity growth that we see.

In our simulations, binary hardening rates  $s$  are essentially constant with time. If we assume that this remains true beyond the end of our simulations, we can use equations (11) and (15) to extrapolate the binary elements ( $a, e$ ) to arbitrarily later times. At some point, gravitational wave emission will dominate the evolution; calculating when this happens requires assigning physical units to the models. We considered two representative scalings, based on assumed MBH masses of  $4.0 \times 10^6 M_\odot$  and  $10^8 M_\odot$  respectively. Scaling factors for length were set at 10 pc and 40 pc respectively, yielding physical values of the influence radii of  $\sim 3$  pc and  $\sim 12$  pc. As discussed in Section 3, the unit of time is determined in this (full loss cone) regime by orbital periods, not relaxation times; hence the scaling factor for time,  $[T]$ , is related to the scaling factors for mass and length by  $[T] = \sqrt{[L]^3/(G[M])}$  and the binary hardening rate in physical units is  $[L]^{-1} [T]^{-1}$  times the  $N$ -body hardening rate.

Given a value for  $s$ , and scale factors for mass and length, the evolution of the binary semi-major axis at late times is determined by

$$\frac{da}{dt} = \left. \frac{da}{dt} \right|_{\text{SI}} + \left. \frac{da}{dt} \right|_{\text{GW}} = -s a^2(t) + \left. \frac{da}{dt} \right|_{\text{GW}} \quad (17)$$

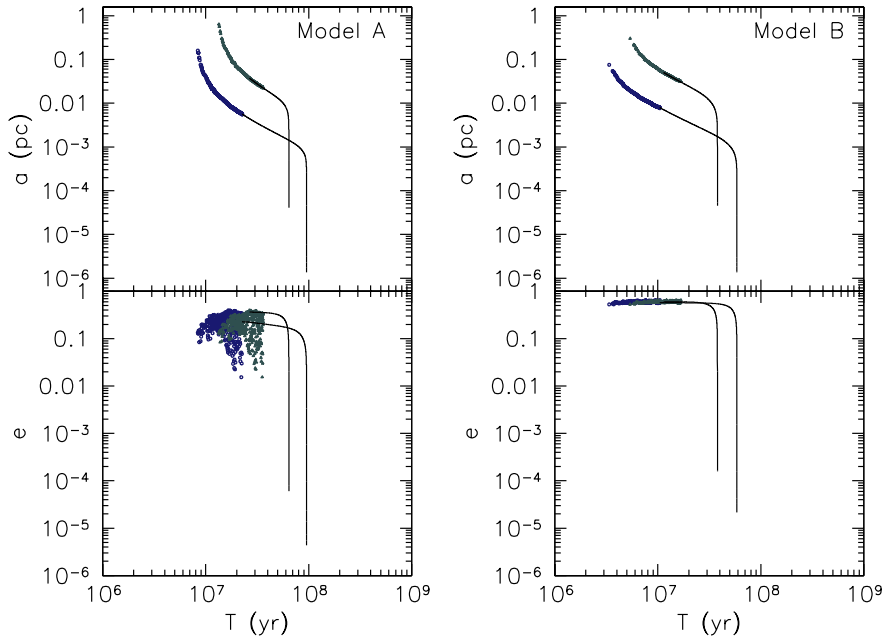


FIG. 10.— Evolution of the binary elements in the  $N$ -body phase (symbols) and in the semi-analytic phase (lines). For each model, two physical scalings are adopted, as discussed in the text.

TABLE 3  
HARDENING PHASE PARAMETERS

Model	$M_1$ ( $M_\odot$ )	$T_{\text{NB}}$ (yr)	$T_{\text{HD}}$ (yr)	$a_f$ (mpc)	$e_f$	$e_g$
A	$4 \times 10^6$	$2.3 \times 10^7$	$7.3 \times 10^7$	5.6	0.23	$8 \times 10^{-6}$
	$1 \times 10^8$	$2.7 \times 10^7$	$3.7 \times 10^7$	37.2	0.37	$8 \times 10^{-5}$
B	$4 \times 10^6$	$1.0 \times 10^7$	$4.8 \times 10^7$	8.0	0.58	$4 \times 10^{-5}$
	$1 \times 10^8$	$1.1 \times 10^7$	$2.6 \times 10^7$	50.2	0.60	$2 \times 10^{-4}$

where the first term on the right hand side represents hardening due to interactions with stars, and the second term represents energy lost to gravitational waves. The rate of the latter process depends on  $e$  as well as  $a$ . In extrapolating  $e$  beyond the end of the  $N$ -body integrations, we ignored the effect of the galaxies' rotation on the binaries' eccentricity growth and simply applied equations (15) and (16). The rate of change of the orbital elements due to GW emission is (Peters 1964)

$$\left. \frac{da}{dt} \right|_{\text{GW}} = -\frac{64}{5} \beta \frac{F(e)}{a^3} \quad (18a)$$

$$\left. \frac{de}{dt} \right|_{\text{GW}} = -\frac{304}{15} \beta \frac{eG(e)}{a^4} \quad (18b)$$

where  $F(e)$  is given in equation (11),

$$G(e) = (1 - e^2)^{-5/2} \left( 1 + \frac{121}{304} e^2 \right) \quad (19)$$

and

$$\beta = \frac{G^3}{c^5} M_1 M_2 (M_1 + M_2) .$$

We numerically solved the coupled equations for the evolution of the semi-major axis and eccentricity, start-

ing from values at the end of the  $N$ -body phase or somewhat earlier, for each of the two sets of scaling factors. The results are shown in Figure 10 and Table 3. In this table, the time  $T_{\text{NB}}$  represents the time spent in the  $N$ -body hardening phase while  $T_{\text{HD}}$  represents the time from the end of the  $N$ -body integration until coalescence; the latter time includes both a stellar-interaction driven, and a GW dominated, regime. The total evolution time from the beginning of the galaxy merger to full coalescence is given by the sum of the two times. For a Milky Way type galaxy undergoing a 3 : 1 merger, this time is of the order of  $10^8$  yr for an initial circular orbit and  $6 \times 10^7$  yr for an initially moderately eccentric orbit. The table also lists the values of the semi-major axis  $a_f$  and eccentricity  $e_f$  at the transition between the simulated  $N$ -body phase and the semi-analytical phase, as well as the value of the eccentricity when the separation reaches  $10r_g = 10GM_1/c^2$ . At smaller separations, equations like (18) are not valid.

#### 4.2. Core formation

The pre-merger galaxies had central density profiles that were well approximated as power laws with respect to radius. Following the merger, the density on scales  $r \lesssim r_h$  is strongly modified (lowered) by the action of the massive binary. The process of “core scouring” is illustrated in Figure 11, which compares the spatial density profiles of the different species in the larger galaxy at four different times. For this plot, only particles that were originally associated with the larger galaxy were used. By the time the binary has become hard, a mass deficit (Milosavljević et al. 2002) is clearly visible in all components on scales significantly larger than  $r_m$ . Model A shows substantially more evolution of the central density at early times; at late times the cores in the two models are more similar.

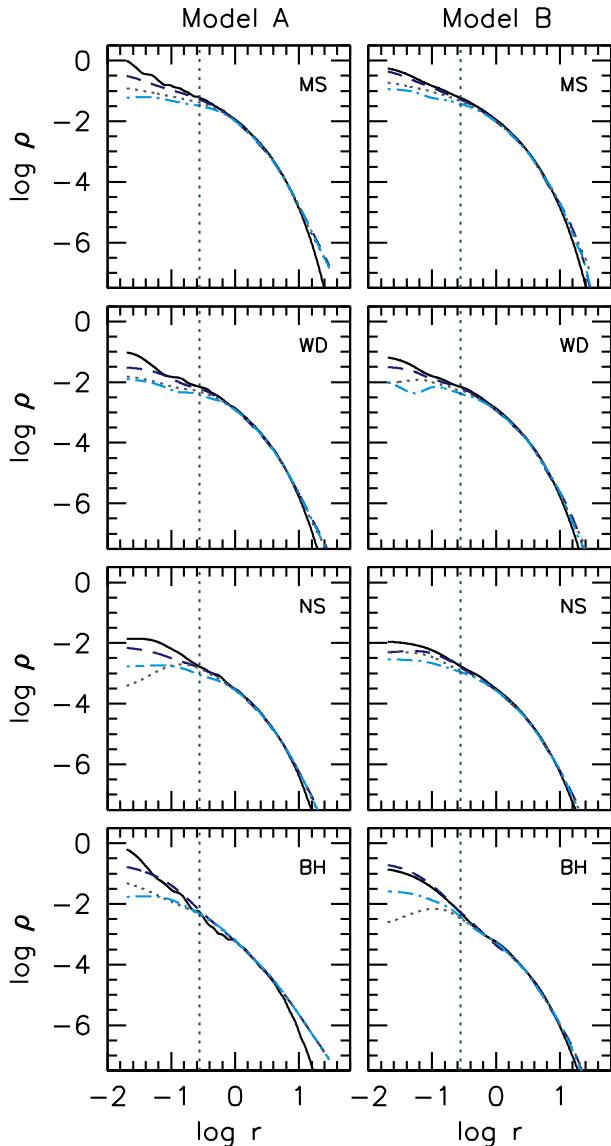


FIG. 11.— Spatial density profiles of the different mass groups in the larger galaxy. For each species, different lines are for different times during the merger phase: at the start of the simulation (solid lines), at the time when  $a \sim a_f$  (dashed lines), at the time when  $a \sim a_h$  (dotted lines) and at a late time when  $a \sim 0.1a_h$  (dashed-dotted lines). Vertical lines indicate  $r_m$ , defined as described in the text.

We estimated core sizes in two ways. First, we fit core-Sérsic profiles to our models at the end of the merger phase, and adopted the resulting values of the break radius  $R_b$  as estimates of the core radius. The projected density profiles of galaxies are globally well fit by the Sérsic (1968) law:

$$I(R) = I(0) \exp \left\{ -b (R/R_e)^{1/n} \right\} \quad (20)$$

where  $I(0)$  is the central intensity,  $R_e$  is the effective half-light radius, and  $n$  is a parameter controlling the curvature in a log-log plot. The term  $b$  is not a parameter but a function of  $n$  (see e.g. Terzić & Graham 2005). Deviations from this law appear close to the center, where bright galaxies typically show central light deficits with respect to the inward extrapolation of the

TABLE 4  
CORE RADII

Model	$r_m$	$R_b$ (MS)	$r_c$ (MS)	$R_b$ (BH)	$r_c$ (BH)
A	0.38	2.4	0.8	5.1	0.3
B	0.36	0.9	0.6	3.5	0.2

Sérsic law while faint galaxies show central light excesses (e.g. Graham & Guzmán 2003; Ferrarese et al. 2006b; Côté et al. 2007). Adding an inner power-law with slope  $\gamma$  (Graham et al. 2003) yields

$$I(R) = I' [1 + (R_b/R)^\alpha]^\gamma \exp \left\{ -b (R^\alpha + R_b^\alpha) / R_e^\alpha \right\}^{1/(n\alpha)} \quad (21)$$

with

$$I' = I_b 2^{-\gamma/\alpha} \exp \left[ b 2^{1/(\alpha n)} (R_b/R_e)^{1/n} \right], \quad (22)$$

the so-called core-Sérsic law. Here,  $\alpha$  is an additional parameter regulating the transition from the inner power-law to the outer Sérsic law and  $R_b$ , the break radius, marks the distance where the profile changes from one regime to the other.

We also considered a second definition of the core radius (King 1962), as the projected radius  $r_c$  at which the surface density falls to one-half its central value. Here, “central” was taken to be the value at a projected radius of  $0.1r_m$ .

Both estimates, computed at the time when  $a \sim 0.1a_h$ , are listed in Table 4, separately for the MS stars and the stellar-mass BHs. These radii were computed using *all* the particles from the respective mass groups, without regard to the galaxy with which they were originally associated. We also give  $r_m$ , computed using equation (6); we set  $M_\bullet = M_1 + M_2$  in that equation, and combined together *all* the stellar species from *both* galaxies when computing  $M_\star$ .

In the case of the dominant (MS) mass component, Table 4 shows that  $r_c \approx 2r_m$  for both Models A and B. However,  $R_b$  is somewhat larger than  $r_c$ . The reason is that, due to the flatness of the profile, the radius at which the inner profile transitions to the outer profile (i.e. the break radius) is much larger than the radius at which the density falls to half its central value (i.e. the core radius). This is illustrated in Figure 12 for Model B.

In what follows, we will adopt  $r_c$  as the more robust measure of the core radius. We emphasize that the size of the core in the MS stars is larger than the influence radius of the massive binary in both of our models, whichever definition of “core radius” or “influence radius” is used. One important consequence, discussed in more detail below, is that regrowth of a Bahcall-Wolf cusp at radii  $\lesssim r_m$  following coalescence of the two MBHs leaves the core structure essentially unchanged.

#### 4.3. Stellar ejections

Stars can become unbound during a galaxy merger due to both tidal stripping in the early phases of the merger and gravitational slingshot interactions with the binary MBHs when this is hard. Unbound stars at the end of the merger phase are a result of both mechanisms. We determined the number of unbound stars in the two merger simulations by selecting stars with velocity in excess of the local escape speed from the system.

TABLE 5  
 FRACTION OF UNBOUND STARS

Model	$f_e$	$f_{e1}$	$f_{e2}$	$f_{eMS}$	$f_{eWD}$	$f_{eNS}$	$f_{eBH}$	$M_{eTS}/M_{gal}$	$M_{eGS}/M_{\bullet}$
A	0.021	0.005	0.016	0.021	0.020	0.024	0.024	0.018	0.55
B	0.014	0.001	0.013	0.014	0.012	0.016	0.018	0.012	0.45

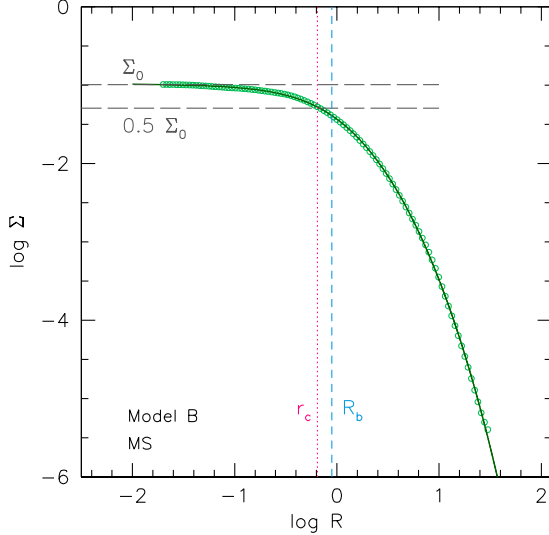


FIG. 12.— Projected density profile for MS stars in Model B, at the time when  $a \sim 0.1 a_h$  (points), with superimposed the best fitting core-Sersic model (solid line). The vertical dotted line indicates  $r_c$  while the vertical dashed line indicates  $R_b$ . The horizontal lines indicate the value of the central density  $\Sigma_0$  and half the central density.

At any given time, the escape velocity at a distance  $r$  from the binary center of mass is  $V_{esc}(r) = \sqrt{-2\Phi(r)}$ , where the gravitational potential  $\Phi$  can be expressed as (Binney & Tremaine 1987, equation 2-22)

$$\Phi(r) = \Phi(r' < r) + \Phi(r' > r) \quad (23)$$

with

$$\Phi(r' < r) = -4\pi G \frac{1}{r} \int_0^r \rho(r') r'^2 dr' \approx \frac{-GM(< r)}{r} \quad (24)$$

having defined  $M(< r)$  the mass enclosed within a sphere of radius  $r$ , and

$$\Phi(r' > r) = -4\pi G \int_r^\infty \rho(r') r' dr' \approx -G \sum_{i=1}^N \frac{m_i}{r_i}, \text{ for } r_i > r. \quad (25)$$

Table 5 reports the total fraction of unbound stars  $f_e$  at the time when  $a \sim 0.1 a_h$ , the fraction of unbound stars originally belonging to the first and second galaxy  $f_{e1}$ ,  $f_{e2}$ , and the fraction of unbound MS, WD, NS and BHs  $f_{MS}$ ,  $f_{WD}$ ,  $f_{NS}$ ,  $f_{BH}$ , normalized to the total number of stars in their mass group. We find that about 2% of all stars are ejected by the end of the merger phase. Model A, which has a more gradual evolution, produces more unbound stars than Model B. Stars from the different mass groups show roughly equal probabilities of being ejected.

We distinguished stars ejected via tidal stripping (TS) versus gravitational slingshot (GS) based on the time they become unbound: if a star becomes unbound before the binary has become hard we consider it ejected by TS whereas if it becomes unbound after the binary has become hard we consider it ejected by GS. Based on this selection, we find that TS is responsible for the ejection of about 90% of the escapers. The smaller galaxy is the most susceptible to TS, as shown by the fact that  $f_{e2} \gg f_{e1}$ . Table 5 also lists the mass in stars unbound by TS in units of the total stellar mass  $M_{gal}$  and by the mass in stars unbound by GS in units of the binary mass. High velocity escapers, with velocities as high as several times the central escape speed, are mainly produced by GS. These stars are analogs of the hyper-velocity stars detected in the halo of the Milky Way (e.g. Brown et al. 2005, 2006; Gualandris et al. 2005; Gualandris & Portegies Zwart 2007; Gvaramadze et al. 2009). Stars unbound by TS tend to have lower velocities, and would be less numerous in a real galaxy, due to the deeper potential well.

## 5. POST-MERGER EVOLUTION

After the two MBH particles were combined into one, we continued the integrations of the  $N$ -body models for several relaxation times. The relaxation time of a multi-component system is ill-defined. We are primarily interested in the time scale for collisional evolution of the dominant population, the MS stars. As a simple estimate of the relaxation time, we used equation (7), setting  $m$  to the mass  $m_{MS}$  of a MS particle, and replacing the number density  $n$  by a simple summation,  $n_t = n_{MS} + n_{WD} + n_{NS} + n_{BH}$ . Other reasonable definitions of  $T_r$  were found to give nearly identical numerical values, a consequence of the fact that the MS stars dominate the total numbers at the radii of interest, and the fact that the masses of the three major groups (MS, NS, WD) are very similar. The resulting estimates of  $T_r$ , computed at the MBH influence radius  $r_m$  at the beginning of the post-merger phase, are given in Table 6. For the Coulomb logarithm we used  $\ln \Lambda = \ln(r_h \sigma^2 / 2Gm_{MS}) = \ln(M_{\bullet} / 2m_{MS})$ , with  $r_h = GM_{\bullet} / \sigma^2$  and  $M_{\bullet}$  the mass of the merged MBHs.

Ignoring the influence of the other components, a cusp in the MS stars is expected to re-form in a time of roughly  $T_r(r_m)$ , at radii  $r \lesssim 0.2 r_m$ , after being destroyed by the massive binary (e.g. Merritt & Szell 2006). In the case of the BHs, their central density should increase more rapidly, by a factor  $\sim m_{BH} / m_{MS} = 10$ , as they segregate spatially with respect to the lighter components. If the density in the heavier (BH) component should ever approach locally the density in the lighter components, heating of the light particles by the heavy particles will occur, causing the density of the former to decrease.

Figure 13 shows the evolution of the enclosed mass in each species in the post-merger integrations. Within the influence sphere, the general trend is for the mass in the

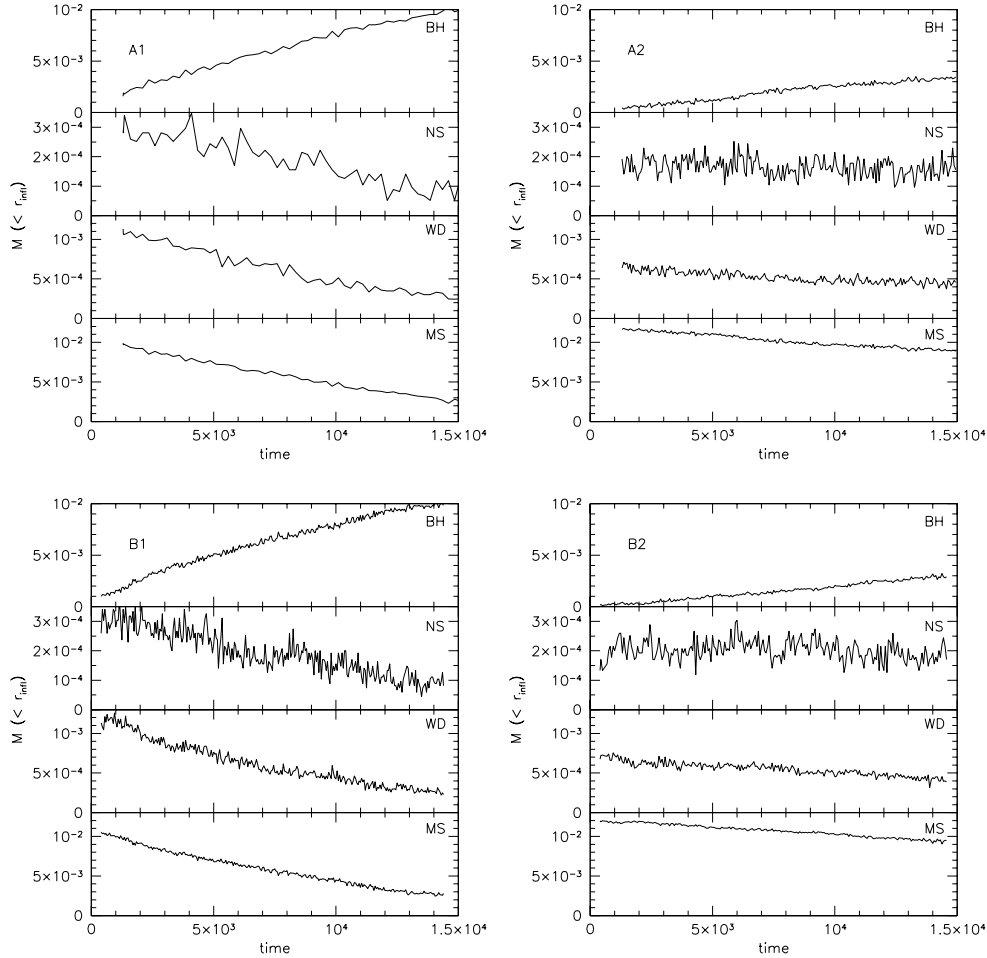


FIG. 13.— Time evolution of the stellar mass enclosed in the MBH influence sphere, for each species, in the post-merger models.

TABLE 6  
CENTRAL PROPERTIES AT THE START OF THE POST-MERGER PHASE

Model	$r_h$	$r_m$	$\ln \Lambda$	$T_r(r_m)$
A1	0.09	0.40	6.4	$4.7 \times 10^3$
A2	0.09	0.43	6.4	$5.8 \times 10^3$
B1	0.09	0.35	6.4	$3.8 \times 10^3$
B2	0.09	0.37	6.4	$3.7 \times 10^3$

lighter components to decrease with time, while the mass in BHs increases. The mass in NSs decreases in models A1 and B1 while it appears nearly constant in models A2 and B2. In terms of mass density, Figure 14 shows that the BHs quickly (on a time scale  $\lesssim T_r(r_m)$ ) form the expected, steep density profile,  $\rho \sim r^{-2}$ . However, the MS stars maintain a core-like profile. Only at very small radii,  $r \lesssim 0.2r_m$ , does evolution toward a cusp appear to occur in the lighter species.

These results are reasonable. In single-component models, a Bahcall-Wolf cusp only extends outward to a fraction of  $r_m$ ; one would not expect the pre-existing MS core to disappear, since it extends well beyond  $r_m$ , where the relaxation time is considerably longer than its value at  $r_m$ . Furthermore, heating by the heavier BHs should cause the mean density of the lighter species to decrease

with time, as observed.

However, at first blush, the results shown in Figures 13 and 14 seem to contradict the results described by Preto & Amaro-Seoane (2010), who used Fokker-Planck and  $N$ -body integrations to follow the evolution of models with two mass species and a MBH. Those authors stated that “mass segregation...speeds up cusp growth [in the lighter component] by factors ranging from 4 to 10 in comparison with the single-mass case.” Preto & Amaro-Seoane (2010) concluded that relaxation to a mass segregated, collisional steady state takes place in a time much less than the relaxation time at the influence radius, hence that collisionally-relaxed models like that of Hopman & Alexander (2006) should be a good description of nuclei like that of the Milky Way (in spite of the fact that the Milky Way is not observed to contain a Bahcall-Wolf cusp in the stars).

The initial conditions adopted by Preto & Amaro-Seoane (2010) were rather different than in our post-merger models: our models have bona-fide cores, while their initial models had density cusps,  $\rho \sim r^{-\gamma}$  with  $\gamma = (1/2, 1)$ . Nevertheless, the “acceleration” that they describe might be expected to occur also in our models.

To understand the nature of this apparent discrepancy,

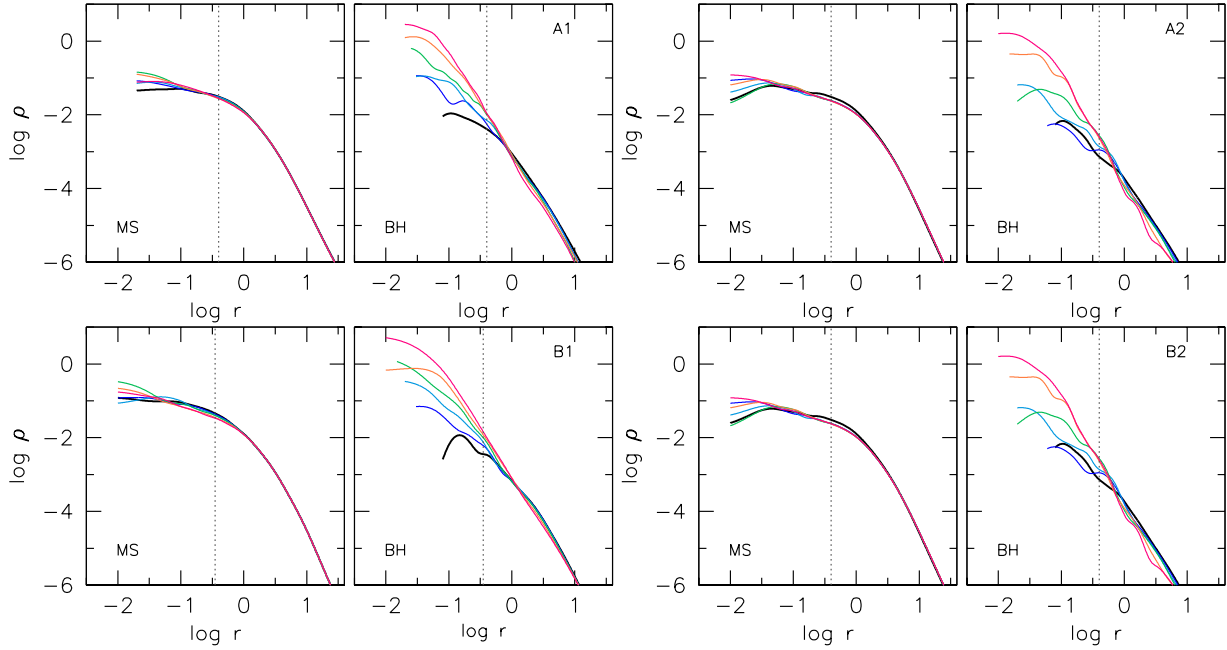


FIG. 14.— Density profiles for MS stars and BHs at different times (0,2,0.5,1,2,3)  $T_r$  during the post-merger phase. Thick solid lines indicate profiles at the beginning of the post-merger phase. Dotted lines indicate  $r_m$ .

we carried out a number of separate  $N$ -body experiments, as well as Fokker-Planck integrations. The latter are presented in the next sub-section.

We first checked whether our  $N$ -body code would reproduce the rate of cusp formation observed by other authors in single-component models. The left panel of Figure 15 shows the evolution of model C1, which had the same initial density profile and MBH mass as “Run 1” of Preto et al. (2004), and  $N = 131072$ . A  $\rho(r) \sim r^{-7/4}$  density cusp forms in roughly one relaxation time at radii  $r \lesssim 0.5r_m$ , and the time dependence of the density is in excellent agreement with what was found in that paper and in other  $N$ -body studies (e.g. Baumgardt et al. 2004). Additional experiments, varying the softening length, time step and particle number, convinced us of the robustness of this result.

The right panels of Figure 15 show the results of integrating a two-component model, C2, with the same initial conditions as “Run 1” of Preto & Amaro-Seoane (2010), and  $N = 131072$ . Cusp growth is clearly observed only in the heavier component, similar to what we described above in the  $N$ -body integrations of the four-component A and B. Again in this case, additional experiments using different integration parameters confirmed the results.

### 5.1. Fokker-Planck models

We carried out integrations of the isotropic Fokker-Planck equation describing galaxies containing two stellar mass groups and a MBH. We used these integrations to address two questions. (1) What is the nature of the “accelerated cusp growth” that Preto & Amaro-Seoane observed in their Fokker-Planck integrations? (2) Is the evolution that we observe in our multi-component  $N$ -body models consistent with the predictions of Fokker-Planck models?

We begin by summarizing the evolution equations.<sup>3</sup>

Let  $f_i(E, t)$  be the phase-space number density of the  $i$ -th species at time  $t$  and (binding) energy  $E$ , where  $E = -v^2/2 + \psi$  and  $\psi = -\Phi$  with  $\Phi$  the gravitational potential. Let  $i = 1$  denote main-sequence stars, of mass  $m_1$ , while  $i = 2$  denotes stellar-mass BHs, of mass  $m_2$ ; we set  $m_2/m_1 = 10$  as in the  $N$ -body integrations. The evolution equation for the  $i$ -th component is

$$4\pi^2 p(E) \frac{\partial f_i}{\partial t} = -\frac{\partial F_i}{\partial E} \quad (26a)$$

$$F_i = \sum_{j=1,2} \left( -D_{EEij} \frac{\partial f_i}{\partial E} - D_{Eij} f_i \right) \quad (26b)$$

$$D_{EEij} = 16\pi^3 \Gamma m_j^2 \left[ q(E) \int_0^E f_j(E', t) dE' + \int_E^\infty f_j(E', t) q(E') dE' \right] \quad (26c)$$

$$D_{Eij} = -16\pi^3 \Gamma m_i m_j \int_E^\infty f_j(E', t) p(E') dE' \quad (26d)$$

(Merritt 2012). Here,  $p(E)$  and  $q(E)$  are given by

$$p(E) = 4 \int_0^{\psi^{-1}(E)} r^2 v(E, r) dr, \quad (27a)$$

$$q(E) = \frac{4}{3} \int_0^{\psi^{-1}(E)} r^2 v^3(E, r) dr \quad (27b)$$

with  $\psi^{-1}(E)$  the inverse of the potential function,  $v(E, r) = \sqrt{2[\psi(r) - E]}$ , and  $\Gamma = 4\pi G^2 \ln \Lambda$ . To

<sup>3</sup> These equations differ from the similar equations given by Preto & Amaro-Seoane (2010); the latter appear to be missing some multiplicative factors, as well as having an incorrect dependence of the diffusion coefficients on the  $m_j$ . However, we believe that their numerical implementation was based on the equations in their correct form.

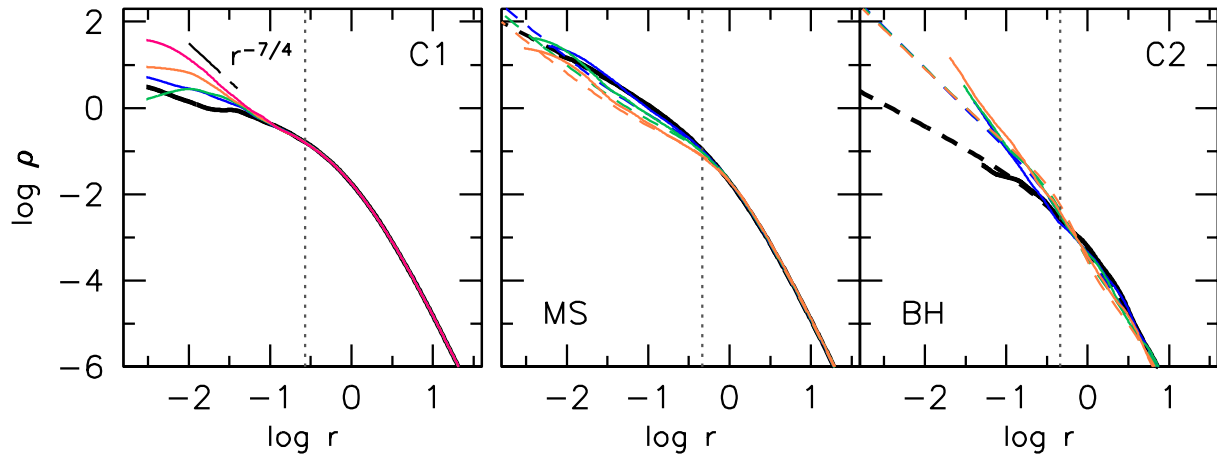


FIG. 15.— Left: Density profiles in the single mass model C1 at different times:  $(0, 0.25, 0.5, 1, 2) T_r(r_m)$ . The thick line indicates the initial profile. Right: Density profiles in the two-component model C2 at different times:  $(0, 0.25, 0.5, 1) T_r(r_m)$ . Solid lines are from the  $N$ -body integrations while dashed lines are FP models. Vertical dotted lines indicate  $r_m$  in all panels.

simplify the calculations, we made the assumption (as in numerous earlier studies e.g. Preto et al. 2004; Merritt et al. 2007a; Preto & Amaro-Seoane 2010) that the gravitational potential,

$$\psi(r) = \frac{GM_\bullet}{r} + \psi_\star(r), \quad (28)$$

the sum of the stellar and MBH potentials, was constant with time, and given by its value at  $t = 0$ . This is a reasonable approximation at all radii: even if the stellar density evolves significantly at  $r \lesssim r_m$ , the potential at these radii is dominated by the MBH and is nearly unchanging. At  $r \gtrsim r_m$  there is no significant evolution in the density and the approximation is again valid.

The coupled equations (26) were solved by standard techniques, starting from initial conditions in which the two components had configuration-space densities

$$\rho_i(r) = \rho_i(0) \left(\frac{r}{r_0}\right)^{-\gamma} \left(1 + \frac{r}{r_0}\right)^{\gamma-4} \quad (29)$$

with the same  $(r_0, \gamma)$ . This is the same initial mass distribution adopted by Preto & Amaro-Seoane (2010), who set  $\gamma = (1/2, 1)$ . Parameters defining the initial conditions were  $\gamma$ ;  $M_\bullet/M_{\text{gal}}$ , the ratio of MBH mass to the total mass in components 1 and 2; and the number density ratio

$$\mathcal{R} \equiv \frac{N_{\text{BH}}}{N_{\text{MS}}}. \quad (30)$$

As unit of time we adopted the relaxation time defined above, evaluated at the MBH influence radius  $r_m$ , with  $r_m$  defined as in the  $N$ -body models; note that the value of  $\log \Lambda$  becomes irrelevant when the time is expressed in this way.

The right panels of Figure 15 show results from a Fokker-Planck integration of the same initial conditions used for the  $N$ -body model C2 described above. The agreement is very good.

Figure 16 shows integrations of two models both with  $\gamma = 0.5$  and  $M_\bullet/M_{\text{gal}} = 0.05$ . The models differ in the fraction of heavy objects:  $\mathcal{R} = 0$  and  $\mathcal{R} = 10^{-3}$ . The model with  $\mathcal{R} = 10^{-3}$  is the same model plotted by Preto & Amaro-Seoane (2010) in their Figure 3. We

have plotted only the density of the lighter (MS) component.

The superficial appearance of these plots depends strongly on the radial range plotted. If the range is sufficiently large, extending to radii  $\ll r_m$ , a MS cusp with slope  $d \log \rho / d \log r \approx -3/2$  catches the eye in the model with BHs. This is the feature emphasized by Preto & Amaro-Seoane (2010). Viewed more closely, in the region  $0.02 \lesssim r/r_m \lesssim 1$ , the plots tell a different story: the model including BHs exhibits a *lower* density in MS stars at all times. Excepting at very small radii, addition of the BHs has the expected effect of reducing the density of the MS stars.

Preto & Amaro-Seoane (2010) attributed the “accelerated cusp growth” in the lighter component to “mass segregation,” without stating explicitly the connection between the two phenomena. In fact, as we now argue, the mechanism driving the evolution of the lighter component at small radii is not mass segregation; it is scattering of the light component by the heavy component (Merritt et al. 2007a; Alexander & Hopman 2009).

Consider a two-component system; as before, species no. 1 is the light (MS) component and species no. 2 is the heavy (BH) component. The four diffusion coefficients that appear in the Fokker-Planck equation for the light (MS) component scale with  $m_i$  and  $f_i$  as

$$\begin{aligned} D_{EE_{11}} &\simeq m_1^2 f_1 \simeq m_1 \rho_1, & D_{E_{11}} &\simeq m_1^2 f_1 \simeq m_1 \rho_1 \\ D_{EE_{12}} &\simeq m_2^2 f_2 \simeq m_2 \rho_2, & D_{E_{12}} &\simeq m_1 m_2 f_2 \simeq m_1 \rho_2. \end{aligned}$$

If  $m_2 \rho_2 \gg m_1 \rho_1$ ,  $D_{EE_{12}} \gg D_{EE_{11}}$ ; in other words, self-scattering is negligible compared with scattering off of BHs. The first-order coefficients are smaller than  $D_{EE_{12}}$  by factors of  $(m_1 \rho_1)/(m_2 \rho_2)$  and  $m_1/m_2$  and can also be ignored. The evolution equation for the light component becomes in this limit

$$\frac{\partial f_{\text{MS}}}{\partial t} \approx \frac{1}{4\pi^2 p} \frac{\partial}{\partial E} \left( D_{EE} \frac{\partial f_{\text{MS}}}{\partial E} \right) \quad (31)$$

with  $D_{EE}$  given by equation (26c) after setting  $m_j = m_{\text{BH}}$ . The steady-state solution is obtained by setting

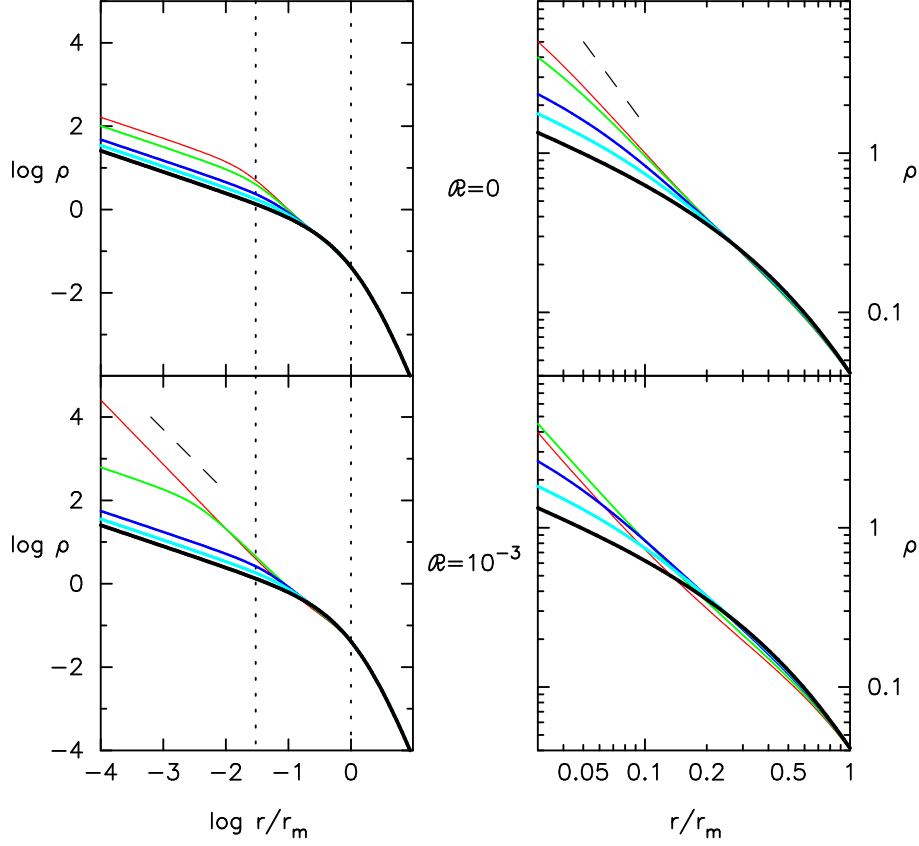


FIG. 16.— Density profiles of the lighter (MS) component in Fokker-Planck integrations of two, two-component models; the heavier component, the BHs, are assumed to have masses ten times the mass of a MS star. The initial conditions differ only in terms of the fraction of heavy particles:  $\mathcal{R} = N_{\text{BH}}/N_{\text{MS}} = 0$  (top) and  $10^{-3}$  (bottom). Both components have  $\gamma = 0.5$  initially, a “core,” and  $M_{\bullet}/M_{\text{gal}} = 0.05$ . The model with  $\mathcal{R} = 10^{-3}$  is the same model plotted in Figure 3 of Preto & Amaro-Seoane (2010), as an illustration of “accelerated cusp growth;” times shown are also the same as in that figure, i.e.,  $t = (0, 0.05, 0.1, 0.2, 0.25)$  in units of the relaxation time at the influence radius. Panels on the left show the MS density profile at low spatial resolution, while panels on the right focus in on the region nearer  $r_m$ ; the dotted lines on the left delineate the region plotted on the right and the dashed lines have logarithmic slopes of  $-7/4$  (right) and  $-3/2$  (left). The accelerated cusp growth described by Preto & Amaro-Seoane (2010) is seen to be present only at small radii,  $r \lesssim 0.05r_m$ ; it is due to scattering of the MS stars by the BHs, which causes the initial “hole” in phase space to rapidly fill in. At radii  $r \gtrsim 0.05r_m$ , adding the BHs has the opposite effect, resulting in a lower density of the MS component at all times.

the term in parentheses (the flux) to zero, yielding

$$\frac{\partial f_{\text{MS}}}{\partial E} = 0, \quad f_{\text{MS}} = \text{const} \quad (32)$$

independent of  $f_{\text{BH}}$ . A constant  $f_{\text{MS}}$  corresponds, in a point-mass potential, to a density

$$\rho_{\text{MS}} \propto r^{-3/2}, \quad (33)$$

which describes the MS cusp that appears, at early times and at small radii, in the Fokker-Planck models.

The manner in which this steady state is reached will depend on the initial conditions. In the models considered here, the initial MS density is  $\rho_{\text{MS}} \propto r^{-1/2}$ , which corresponds to an  $f(E)$  that tends to zero near the MBH – a “hole” in phase space at low energies. Scattering of the MS component by the BHs rapidly “fills in” this hole as it drives  $f$  toward a constant value. The result is a sharp increase in the MS density at early times at the smallest radii.

The condition that the evolution of the light (MS) component be dominated by scattering off the heavy (BH) component – as opposed to self-interactions, which tend to build a steeper, Bahcall-Wolf cusp – is

$\rho_{\text{BH}} \gtrsim (m_{\text{MS}}/m_{\text{BH}})\rho_{\text{MS}} \approx 0.1\rho_{\text{MS}}$ . In Figure 17, the first time at which this condition is satisfied is marked by open circles. That figure shows evolution of the local slope,  $|d \log \rho_{\text{MS}}/d \log r|$ , at two radii,  $0.05r_m$  and  $0.002r_m$ , for several different values of  $\mathcal{R}$ , as computed via the Fokker-Planck equation. At the larger radius, the BHs remain a small fraction of the total in most of these models, and the evolution of the MS component is not strongly affected. But because the Bahcall-Wolf cusp builds “from the outside in,” its initial growth is hardly reflected at much smaller radii. Here, as the lower panel shows, the dominant effect is scattering by BHs, and the effect of the scattering on the MS density profile is strongly dependent on (roughly proportional to)  $\mathcal{R}$ .

We summarize our findings in this section as follows.

- 1 One- and two-component Fokker-Planck models reproduce well the behavior seen in  $N$ -body integrations with the same initial parameters.
- 2 In two-component (MS + BH) models, addition of the heavy (BH) component results in a slightly lower MS density at radii  $r \gtrsim 0.05r_m$ , due to heating of the stars by the BHs.



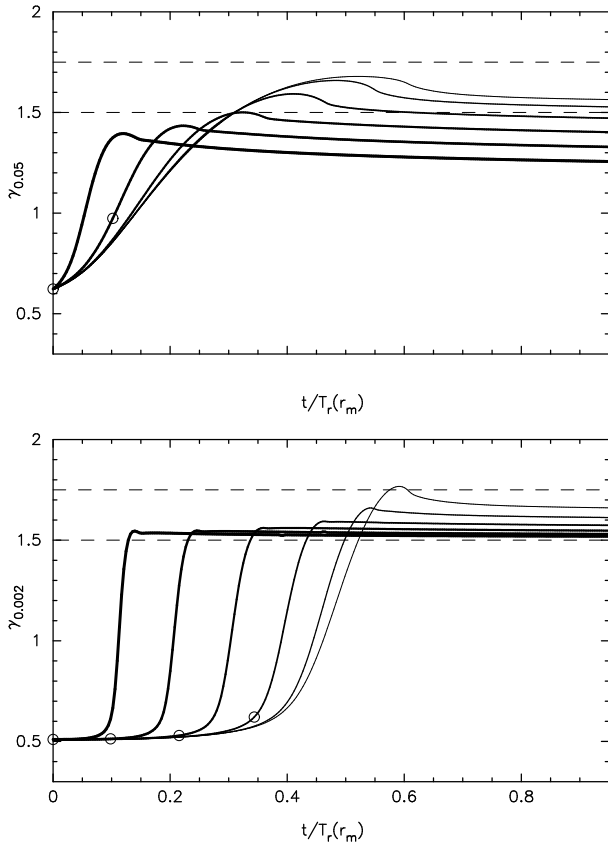


FIG. 17.— Evolution of the local slope,  $\gamma \equiv -d \log \rho / d \log r$ , of the MS density profile, in two-component (MS + BH) Fokker-Planck models like those in Figure 16. The curves differ in terms of the heavy-particle number fraction,  $\log_{10} \mathcal{R} = \log_{10}(N_{\text{BH}}/N_{\text{MS}}) = -7, -6, -5, -4, -3, -2$ ; increasing line width corresponds to increasing  $\mathcal{R}$ . Upper panel shows slopes at  $r = 0.05 r_m$ , bottom panel at  $r = 0.002 r_m$ . Open circles indicate the times at which  $\rho_{\text{BH}} = 0.1 \rho_{\text{MS}}$  at the respective radii. Adding a heavy (BH) component has relatively little effect on the growth of a Bahcall-Wolf cusp in the MS component (top panel), however it greatly affects the form of the density profile at  $r \lesssim 0.01 r_m$  (bottom panel), for the reasons discussed in the text. The latter phenomenon is the “accelerated cusp growth” described by Preto & Amaro-Seoane (2010).

3 The same heating more promptly modifies the MS density profile at small radii,  $r \lesssim 0.05 r_m$ , at least in models that start from a flat core. The rate of growth of this “mini-cusp” is strongly dependent on the BH fraction.

The fact that the effects of scattering of MS stars by BHs is restricted to small radii,  $r \lesssim 0.05 r_m$ , is consistent with the fact that we do not observe this phenomenon in the  $N$ -body simulations: for instance, the density profiles of Figure 14 extend down to only  $\sim 0.05 r_m$ . Only a handful of particles were ever present at smaller radii. At the radii resolvable by the  $N$ -body simulations, the Fokker-Planck models predict that the BHs should *retard* the growth of the Bahcall-Wolf cusp in the MS component (Figure 16), not accelerate it, and this is what we see in the  $N$ -body simulations.

### 5.2. Time dependence of the number of BHs near the MBH

We now return to a discussion of the post-merger  $N$ -body integrations. Figure 13 showed the evolution of the

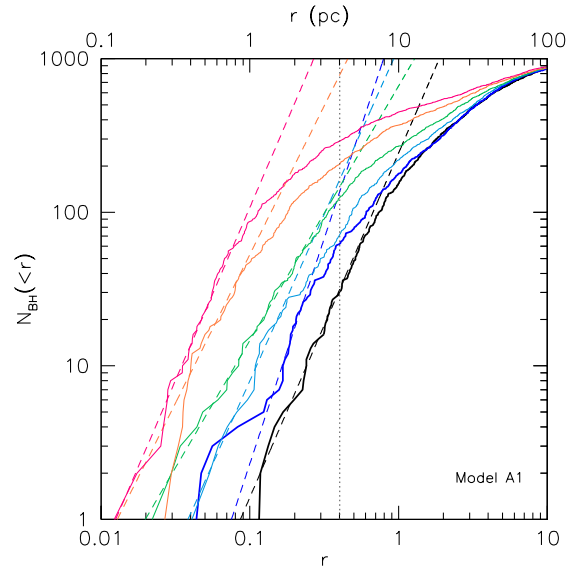


FIG. 18.— Cumulative radial distribution of stellar-mass BHs (solid lines) in Model A1. Different curves refer to different times:  $(0, 0.2, 0.5, 1, 2, 3) T_r$  from right to left, as in Figure 14. The dotted vertical line indicates  $r_m$ . Dashed lines show fits to  $N_{\text{BH}}(<r)$  in the radial range  $[r_1, r_2]$  such that  $N_{\text{BH}}(r_1) = 5$  and  $N_{\text{BH}}(r_2) = 25$ .

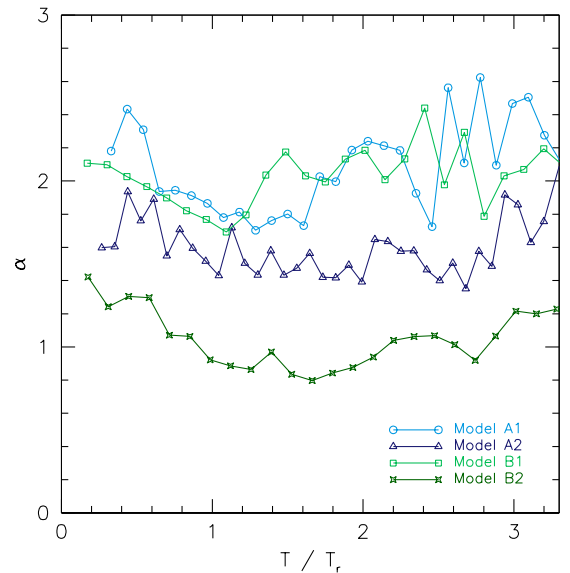


FIG. 19.— Evolution of the slope,  $\alpha \equiv -d \log N_{\text{BH}} / d \log r$ , derived from regression fits to the post-merger  $N$ -body data, as shown in Figure 18 for Model A1. The corresponding density-profile slope is  $\gamma = 3 - \alpha$ .

mass enclosed within  $r_m$  for each of the four species in each of the  $N$ -body integrations. In this section, we look more closely at how the number of BH particles evolves with time on smaller scales.

Figure 18 plots the cumulative radial distribution of BHs in Model A1 at different times. Time zero in this plot corresponds to the moment that the two, MBH particles were combined into one. The smallest radii at which there are any BH particles in the  $N$ -body mod-

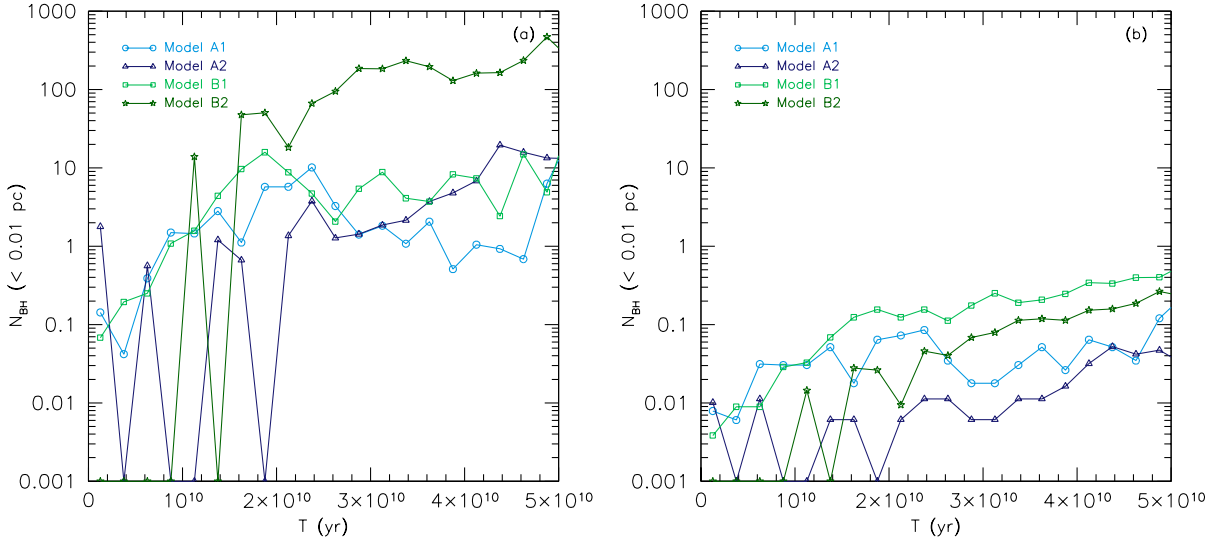


FIG. 20.— Number of stellar-mass BHs within 0.01 pc versus time in our models, scaled to the Milky Way nucleus, assuming (a) a density profile of constant logarithmic slope at small radii, and (b) a constant density inside  $0.1r_m$ .

els decreases from  $\sim 0.1r_m$  at early times to  $\sim 0.01r_m$  at late times. In order to estimate BH numbers at smaller radii, we carried out regression fits of  $\log N_{\text{BH}}$  to  $\log r$ . The fits were performed in the radial interval  $[r_1, r_2]$  such that  $N_{\text{BH}}(< r_1) = 5$  and  $N_{\text{BH}}(< r_2) = 25$ . The resulting slopes,  $\alpha \equiv |d \log N_{\text{BH}} / d \log r|$ , are plotted in Figure 19 for all models as a function of time in units of the initial relaxation time. We find slopes  $1 \lesssim \alpha \lesssim 3$  for  $N_{\text{BH}}(r)$ , which imply slopes in the mass density profile in the range  $0 \lesssim -d \log \rho / d \log r \lesssim 2$ .

Figure 20 shows the inferred number of BHs at  $r < 0.01$  pc as a function of time. In making this plot, we did a rough scaling of our models to the nucleus of the Milky Way, assuming an influence radius  $r_m$  of 3 pc. The factor:

$$\frac{4 \times 10^6 M_\odot}{10 M_\odot} \times \frac{m_{\text{BH}}}{M_\bullet} = 3.3 \times 10^3$$

was used to convert the number of BH particles in the simulations to the actual number; the first of these factors contains masses in physical units, the second in the units of the  $N$ -body code. Since the number of BH particles at these radii is small, we extrapolated inward under two assumptions: a density profile of constant power-law index, and a constant density inside  $r = 0.1r_m$ . In the former case, we used the slopes derived from the fits to  $N_{\text{BH}}(r)$ . Since the fitted slopes are typically large, the former assumption results in much larger, inferred numbers of BHs.

It is tempting to compare the numbers so obtained with estimates of  $N_{\text{BH}}$  obtained from steady-state Fokker-Planck models of the Milky Way nucleus (Hopman & Alexander 2006; Freitag et al. 2006). Here we note one ambiguity associated with such comparisons. In the Milky Way, the two influence radii  $r_h$  and  $r_m$  are

similar. The first is

$$r_h \equiv \frac{G M_\bullet}{\sigma^2} \approx 3.5 \text{ pc} \left( \frac{M_\bullet}{4 \times 10^6 M_\odot} \right) \left( \frac{\sigma}{70 \text{ km s}^{-1}} \right)^{-2}. \quad (34)$$

The second is somewhat less certain, but dynamical estimates of the mass distribution in the inner few parsecs (e.g. Schödel et al. (2009); Oh et al. (2009)) give  $r_m \approx 2$  pc, consistent within a factor of two with  $r_h$ . The near-equality of  $r_h$  and  $r_m$  in the Milky Way is due to the fact that the density profile is similar to that of the singular isothermal sphere,  $\rho \sim r^{-2}$ ; the radius of the Milky Way's core is  $\sim 0.5$  pc, substantially smaller than both  $r_h$  and  $r_m$ . In our post-merger  $N$ -body models, on the other hand, core radii and  $r_m$  are both substantially larger than  $r_h$ . This fact precludes a unique scaling of our models to the Milky Way – at least in the Galaxy's current state. (The Milky Way's core may have been larger in the past (Merritt 2010).)

With this caveat in mind, we assume that  $r_m$  determines the scaling of our models to the Milky Way. Figure 20 is based on this scaling. In their collisionally-relaxed models, Hopman & Alexander (2006) found

$$N_{\text{BH}}(r < 0.01 \text{ pc}) = 150. \quad (35)$$

Those authors assumed a mass function with the same four species as in our models, and with the same relative numbers as in our models A2 and B2 (Table 1). In Figure 20, the inferred number of BHs inside 0.01 pc is very uncertain at the relevant times, i.e.  $t \approx 10^{10}$  yr, fluctuating between zero, and maximum values of  $\sim 1$  (Model A2) and  $\sim 10$  (Model B2). These upper limits are factors of  $\sim 10^2$  and  $\sim 10^1$ , respectively, smaller than in the Hopman & Alexander (2006) models. There is an independent way to reach a similar conclusion. After several relaxation times,  $N_{\text{BH}}(< 0.01 \text{ pc})$  is  $\sim 10$  (Model A2) and  $\sim 100$  (Model B2). These numbers, presumably representing the mass distribution in a near steady-state,

are  $\sim 10$  times larger than their values at  $t = 10^{10}$  yr.

It is interesting that the BH distribution takes so long to reach this (nearly) steady state – a time of at least twice the relaxation time as defined by the dominant (MS) population (Figure 14). This may be due in part to the fact that the MS distribution is also continuously evolving. Another reason is the persistence of a core in the dominant component. Chandrasekhar’s (1943) dynamical friction coefficient, in its most widely-used form (Binney & Tremaine 1987), predicts that the frictional force near a MBH drops essentially to zero if  $\rho(r)$  increases more slowly than  $r^{-1/2}$  toward the center. The (isotropic) phase-space density  $f(E)$  corresponding to that density profile has no stars moving more slowly than the local circular speed, and Chandrasekhar’s formula identifies the frictional force exclusively with field stars moving more slowly than the massive body. This property of the dynamical friction force was automatically incorporated into the Fokker-Planck calculations presented above, since that equation is based on Chandrasekhar’s coefficients in their standard forms (Rosenbluth et al. 1957). In reality, some part of the frictional force in the  $N$ -body simulations will come from stars moving faster than the test star, and including the contribution from these stars keeps the frictional force from falling identically to zero (Antonini & Merritt 2011). Nevertheless, one expects dynamical friction to act more slowly in these models than expected based on the application of standard formulae that neglect the special properties of  $f$ .

## 6. SHAPE AND KINEMATICS OF THE STELLAR SPHEROID

We determined the shape of the merger remnants during the binary hardening phase by computing the axis ratios at different distances from the center. We followed the procedure described in Katz (1991) and Antonini et al. (2009). We selected all particles within a sphere of radius  $d$  centered on the binary center of mass. The axis ratios were then determined from the eigenvalues  $I_{ii}$  of the inertia tensor  $I$  as

$$\xi = \sqrt{I_{11}/I_{\max}}, \quad \eta = \sqrt{I_{22}/I_{\max}}, \quad \theta = \sqrt{I_{33}/I_{\max}} \quad (36)$$

where  $I_{\max} = \max\{I_{11}, I_{22}, I_{33}\}$ . New axis ratios were computed considering only particles enclosed in the ellipsoidal volume having the previously determined ratios, i.e. all particles satisfying the condition  $q_i < d$ , where

$$q_i^2 = \left(\frac{x_i}{\xi}\right)^2 + \left(\frac{y_i}{\eta}\right)^2 + \left(\frac{z_i}{\theta}\right)^2. \quad (37)$$

The last step was iterated until the axis ratios converged. If we define the axes  $a, b, c$  such that  $a > b > c$ , we find that  $c/a$  and  $b/a$  correspond, respectively, to the minimum and intermediate values of  $\xi, \eta, \theta$ . From the axis ratios it is possible to define a triaxiality parameter

$$T = \frac{a^2 - b^2}{a^2 - c^2}, \quad (38)$$

$0 < T < 1$ , such that  $T = 0$  for an oblate spheroid,  $T = 1$  for a prolate spheroid and  $T = 0.5$  corresponds to maximum triaxiality. The ellipticity  $e = \sqrt{1 - c^2/a^2}$  measures the degree of flattening of the system. The axis ratios, triaxiality parameter and ellipticity for models A

and B are shown in Figure 21 as a function of distance from the binary center of mass, at the time when the binary becomes hard. A moderate triaxiality is present in both models at distances of the order of  $1 - 2 r_m$  from the binary center of mass. At larger distances, the models appear axisymmetric with a small flattening in the direction perpendicular to the binary orbital plane. These features persist throughout the hardening phase. The flattening, due to rotation of the merger remnant, is also visible in the isophotes shown in Figure 22, which are computed at the beginning of the post-merger phase.

Rotation is introduced by the merger process, as illustrated by the velocity map in Figure 23 for Model A. The figure shows the direction and magnitude of the velocities in the binary’s orbital plane. By the time the binary reaches the hard binary separation, a well defined rotation pattern has been established.

The departures from spherical symmetry that we observe in the merger models are probably responsible for the efficient hardening of the massive binary (Merritt & Poon 2004; Berczik et al. 2006).

## 7. SUMMARY AND DISCUSSION

### 7.1. (Re-)growth of Bahcall-Wolf cusps in multi-component systems

In galaxies containing a single stellar population, a  $\rho \propto r^{-7/4}$  Bahcall & Wolf (1976) cusp is expected to appear at radii  $r \leq r_{\text{BW}} \approx 0.2r_m$  around the MBH. While the growth time of the cusp is dependent on the initial conditions, simulations starting from a shallow cusp inside  $r_m$  show that the stellar density will have reached an approximate steady state after roughly one relaxation time at  $r_m$ . We presented an example of such evolution in Figure 15.

In nuclei with two mass groups, e.g. solar-mass stars (MS) and  $10 M_\odot$  black holes (BHs), evolution toward a steady state near the MBH depends on the relative numbers and masses in the two groups, as well as on the initial conditions. The results of our  $N$ -body and Fokker-Planck integrations of two-component models were presented in Section 5.1. Figure 17 showed that addition of the BHs reduces slightly the rate of formation of a Bahcall-Wolf cusp in the MS (light) component, and also affects the final value of the density-profile slope, which varies from  $\rho_{\text{MS}} \sim r^{-7/4}$  when  $\rho_{\text{BH}}/\rho_{\text{MS}}$  is small, to  $\sim r^{-3/2}$  as  $\rho_{\text{BH}}/\rho_{\text{MS}}$  is increased (Bahcall & Wolf 1977). In addition, if the initial MS distribution is very flat near the MBH, scattering by the heavier BHs can dominate the evolution of the MS component at early times for  $r \lesssim 0.05r_m$ , converting  $\rho_{\text{MS}} \sim r^{-1/2}$  to  $\rho_{\text{MS}} \sim r^{-3/2}$  at these small radii, even before the Bahcall-Wolf cusp has fully formed at larger radii.

The full galaxy merger simulations presented here allowed us, for the first time, to evaluate the evolution of multi-component nuclei starting from initial conditions that were motivated by a well-defined physical model. Our pre-merger galaxies contained mass-segregated nuclei with four mass components, representing an evolved stellar population. These initial distributions were modified both by the galaxy merger, and by the formation of a MBH binary, which created a large core in each of the components (Figures 7, 11). The core radius of the heaviest (BH) component was somewhat smaller than the

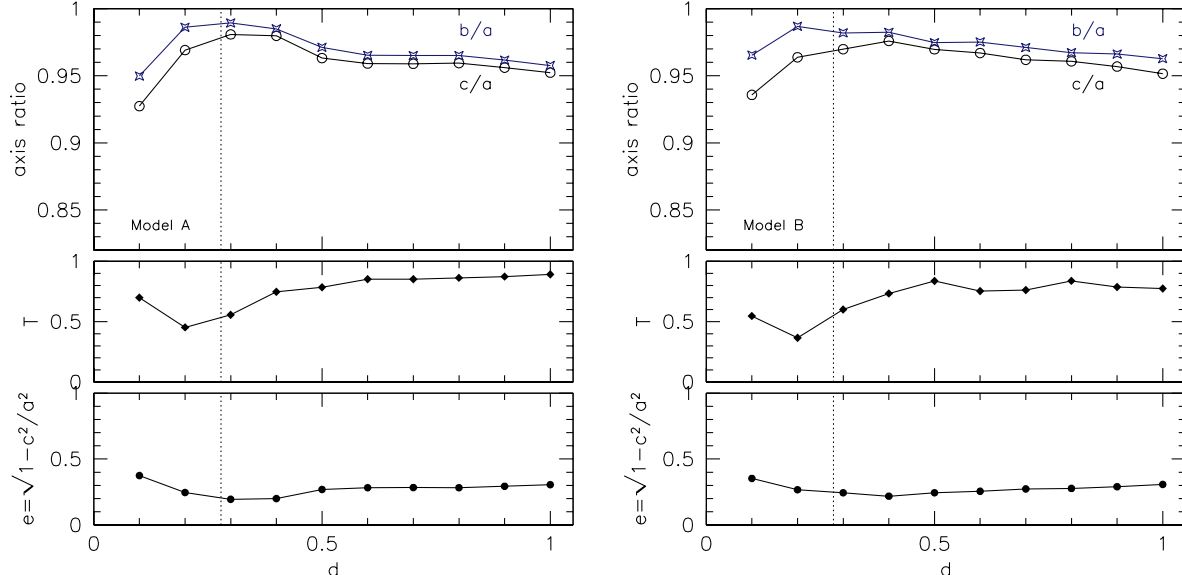


FIG. 21.— Axis ratios, triaxiality parameter and ellipticity for models A (left) and B (right) as a function of distance from the center of the binary, at the time when  $a \sim a_h$ . The vertical lines indicate  $r_m$ .

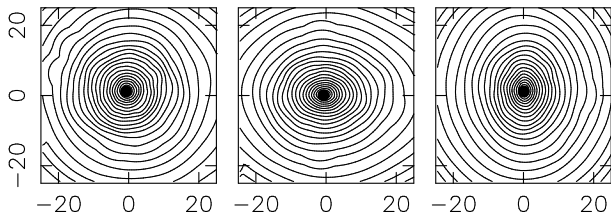


FIG. 22.— Projected density contours for Model B1 at the beginning of the post-merger phase. Left:  $xy$  plane. Middle:  $xz$  plane. Right:  $zy$  plane. The position of the BH is indicated by the filled circle. The merger remnant is flattened in the direction perpendicular to the plane of the merger.

cores in the three lighter components, a relic of the earlier mass segregation, and of the incomplete cusp destruction process during the binary MBH phase (Figure 11). Evolution during the merger phase set the “initial conditions” of the nucleus at the time when the two MBHs were combined into one. Unlike the rather ad hoc initial conditions used in many earlier studies of nuclear evolution (e.g. Freitag et al. 2006; Preto & Amaro-Seoane 2010), our post-merger models have cores that should be reasonable representations of the cores in real galaxies that formed via dissipationless mergers, with mass densities that decline toward the center and anisotropic kinematics that reflect the action of the massive binary on the stellar orbits (Figure 23).

By continuing the evolution of these multi-component models for a time greater than  $T_r(r_m)$  after coalescence of the two MBHs, we found that the cores characterizing the distribution of the dominant, MS component persisted; in fact the MS density at radii  $\sim r_m$  decreased gradually with time (Figure 13) – a predictable consequence of the initial extent of the cores, several times  $r_m$ , implying  $T_r(r_c) > T_r(r_m)$ , and of continued “heating” by the heavier BHs. Nevertheless, a Bahcall-Wolf cusp gradually reformed in the lighter components at radii  $r \lesssim 0.2r_m \ll r_c$ ; growth times were found to be

$\gtrsim T_r(r_m)$ , somewhat greater than in earlier models with more idealized initial conditions (e.g. Freitag et al. 2006).

Our pre-merger galaxies (models A1, B1) contained larger numbers of remnants than would be expected based on a standard IMF; this was done in order to better resolve the distributions of those components near the MBH. We tested the dependence of the *post*-merger evolution on the assumed mass function by carrying out a second set of integrations in which we decreased the relative numbers of remnants (NS, WD, BH) by factors of a few, to values more consistent with standard IMFs (models A2, B2). Evolution of the dominant, MS component in the latter models differed only modestly from its evolution in the models with larger remnant fractions; the main difference was a lower rate of core expansion reflecting a lower rate of heating by the BHs (Figure 13). The rate of growth of the Bahcall-Wolf cusp in the MS component was essentially unchanged (Figure 14).

Our results on the regeneration of Bahcall-Wolf cusps following dissipationless mergers are consistent with those obtained in simulations of single-component galaxies (Merritt & Szell 2006). We can summarize these results by stating that regrowth of a cusp in the dominant stellar component requires a time comparable with, or somewhat longer than, the relaxation time of that component measured at the MBH influence radius. The new simulations presented here suggest that time scales for cusp regrowth are only weakly dependent on the number of heavy remnants (BHs), at least if the fraction of mass in the heavier population does not exceed a few percent of the total.

The Milky Way nucleus is near enough that a Bahcall-Wolf cusp could be resolved if present, and the dominant stellar population is believed to be old. Since  $r_h \approx r_m \approx 2-3$  pc in the Milky Way, the expected, outer radius of the Bahcall-Wolf cusp is  $r_{BW} \approx 0.5$  pc  $\approx 10''$ . As is well known, number counts of the dominant, old stellar population show no evidence of a rise in density

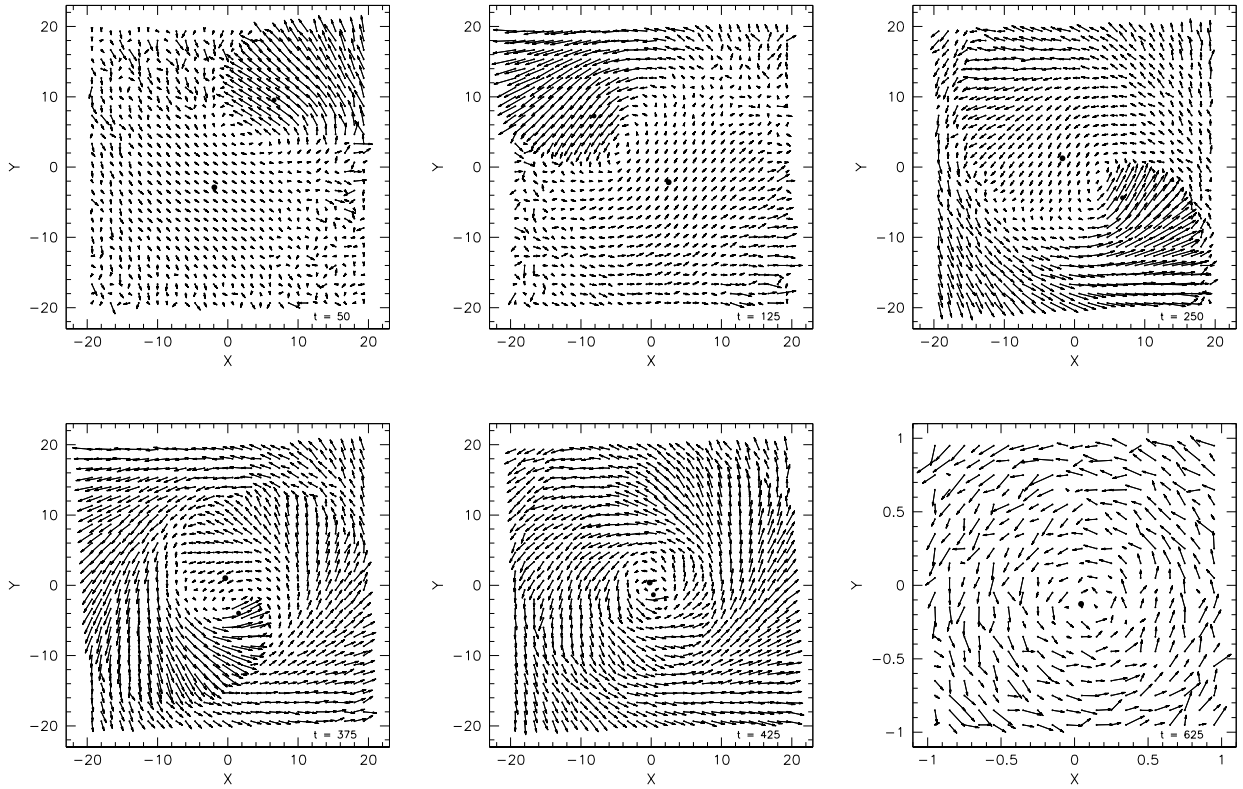


FIG. 23.— Velocity vectors in the orbital plane ( $x - y$  plane) of the binary at different times during the merger of Model A ( $t = 50, 125, 250, 375, 425, 625$ , from the top left to the bottom right). The origin corresponds to the initial position of the binary center of mass. The velocity vectors represent the in-plane velocities of all stars in the chosen area. The circles represent the locations of the massive black holes. The final frame is shown at higher resolution.

at this radius; instead the number counts are flat, or even falling, from  $\sim 10''$  into at least  $1''$  projected radius (Buchholz et al. 2009; Do et al. 2009; Bartko et al. 2010).

Assuming solar-mass stars, the relaxation time at the influence radius of Sgr A\* is 20-30 Gyr (Merritt 2010), while the mean stellar age in the nuclear star cluster is estimated to be  $\sim 5$  Gyr (Figer et al. 2004). The time available for formation of a cusp is therefore  $(5/25)T_r(r_m) \approx 0.2T_r(r_m)$ . Our simulations (e.g. Figure 14) suggest that a Bahcall-Wolf cusp in the dominant component is unlikely to have formed in so short a time, and this is consistent with the lack of a Bahcall-Wolf cusp at the Galactic center.

The core in the Milky Way has a radius of  $\sim 0.5$  pc, somewhat smaller than  $r_h$  or  $r_m$ , while the cores formed in our merger models are somewhat larger than  $r_m$  (Table 4). It has been argued that the Milky Way core is small enough that gravitational encounters would cause it to shrink appreciably in 10 Gyr, as the stellar distribution evolves toward a Bahcall-Wolf cusp (Merritt 2010). The cores in our  $N$ -body models are so large that they do not evolve appreciably after the binary MBH has been replaced by a single MBH; the Bahcall-Wolf cusp forms at radii smaller than  $r_c$ , leaving the core structure essentially unchanged. Without necessarily advocating a merger model for the origin of the Milky Way core (it is unclear whether our galaxy even contains a bulge; Martinez-Valpuesta & Gerhard (2011)), we note that the

sizes of cores formed by binary MBHs scale with the binary mass ratio. Presumably, we could have produced cores more similar in size to the Milky Way's if we had adjusted this ratio.

It has been suggested (Löckmann et al. 2010) that heating by BHs could be responsible for the lack of a Bahcall-Wolf cusp at the Galactic center. We do not find support for this hypothesis, either in our four-component  $N$ -body models, nor in our two-component Fokker-Planck models. The latter showed that even a quite large BH population still allowed a Bahcall-Wolf cusp to form in the MS stars on a time scale of  $\sim T_r(r_m)$ ; the main effect of the BHs is to decrease the asymptotic slope of the cusp from  $\sim r^{-7/4}$  to  $\sim r^{-3/2}$ .

## 7.2. The distribution of massive remnants in galaxy nuclei

A dense cluster of stellar-mass BHs has been invoked as a potential solution to a number of problems of collisional dynamics at the Galactic center. Examples include randomization of the orbits of young stars via gravitational scattering (e.g. Perets et al. 2009), production of hyper-velocity stars through encounters with BHs (e.g. O'Leary & Loeb 2008), and warping of young stellar disks (Kocsis & Tremaine 2011). These treatments typically assume a collisionally-relaxed state for the Galactic center. In the relaxed models, the mass in BHs inside  $0.1$  pc is  $\sim 10^4 M_\odot$ , i.e.  $N_{\text{BH}}(r < 0.1 \text{ pc}) \approx 10^3$  and  $N_{\text{BH}}(r < 0.01 \text{ pc}) \approx 10^2$  (Hopman & Alexander

2006; Freitag et al. 2006), assuming “standard” IMFs. A high density of stellar BHs at the centers of galaxies like the Milky Way is also commonly assumed in discussions of the EMRI (extreme-mass-ratio inspiral) problem (Amaro-Seoane et al. 2007).

Models like these are called into question by the lack of a Bahcall-Wolf cusp in the late-type stars at the center of the Milky Way (Buchholz et al. 2009; Do et al. 2009; Bartko et al. 2010). If the Galactic center is not collisionally relaxed, as these observations seem to suggest, then computing the distribution of the heavy remnants becomes a more difficult, time-dependent problem (Merritt 2010), and knowledge of the initial conditions is essential.

Dissipationless mergers imply “initial conditions” characterized by a core in the dominant stellar component. The cores formed in our (major) merger simulations are large enough that they do not evolve appreciably (i.e. shrink) even after  $\sim 3$  relaxation times at the MBH influence radius. As a result, evolution of the BH distribution takes place against a stellar background with a very different density profile than in the steady-state models. In a core around a MBH, dynamical friction is much weaker than one would estimate by plugging the local density into standard formulae for orbital decay, due to the absence of stars moving more slowly than the local circular velocity (Antonini & Merritt 2011). Scaling our  $N$ -body

models to the Milky Way, we predicted numbers of BHs inside  $r_h$  that were substantially smaller than in the collisionally relaxed models; in the inner  $10^{-2}$  pc – the radii most relevant to the EMRI problem (Merritt et al. 2010) – the number of BHs was, at most, 10-100 times smaller than predicted by these models, even after 10 Gyr (Figure 20).

It is unclear how relevant merger models are to the center of the Milky Way. If the core observed at the Galactic center had some other origin, the distribution of stellar BHs might have little connection with the distribution of the giant stars. However, if cores of size  $r_c \approx r_h$  are common features of galactic nuclei, and if at some early time both the BHs and the stars had a common core radius, our models imply that the distribution of BHs should be considered very uncertain, even in galaxies for which nuclear half-mass relaxation times are as short as the age of the universe.

DM acknowledges support from the National Science Foundation under grants no. AST 08-07910, 08-21141 and by the National Aeronautics and Space Administration under grant no. NNX-07AH15G. We thank Tal Alexander and Eugene Vasiliev for useful discussions.

#### REFERENCES

- Alexander, T. 2005, *Phys. Rep.*, 419, 65  
 Alexander, T., & Hopman, C. 2009, *ApJ*, 697, 1861  
 Amaro-Seoane, P., Gair, J. R., Freitag, M., Miller, M. C., Mandel, I., Cutler, C. J., & Babak, S. 2007, *Classical and Quantum Gravity*, 24, 113  
 Antonini, F., Capuzzo-Dolcetta, R., & Merritt, D. 2009, *MNRAS*, 399, 671  
 Antonini, F., & Merritt, D. 2011, *ArXiv e-prints* 1108.1163  
 Bahcall, J. N., & Wolf, R. A. 1976, *ApJ*, 209, 214  
 —. 1977, *ApJ*, 216, 883  
 Bartko, H., et al. 2010, *ApJ*, 708, 834  
 Baumgardt, H., Makino, J., & Ebisuzaki, T. 2004, *ApJ*, 613, 1133  
 Begelman, M. C., Blandford, R. D., & Rees, M. J. 1980, *Nature*, 287, 307  
 Berczik, P., Merritt, D., & Spurzem, R. 2005, *ApJ*, 633, 680  
 Berczik, P., Merritt, D., Spurzem, R., & Bischof, H.-P. 2006, *ApJL*, 642, L21  
 Binney, J., & Tremaine, S. 1987, *Galactic dynamics*, ed. J. Binney & S. Tremaine  
 Boeker, T. 2010, *The Impact of HST on European Astronomy*, ed. Macchetto, F. D.  
 Brown, W. R., Geller, M. J., Kenyon, S. J., & Kurtz, M. J. 2005, *ApJL*, 622, L33  
 —. 2006, *ApJ*, 647, 303  
 Buchholz, R. M., Schödel, R., & Eckart, A. 2009, *A&A*, 499, 483  
 Côté, P., et al. 2007, *ApJ*, 671, 1456  
 Cuadra, J., Armitage, P. J., Alexander, R. D., & Begelman, M. C. 2009, *MNRAS*, 393, 1423  
 Dehnen, W. 2005, *MNRAS*, 360, 892  
 Do, T., Ghez, A. M., Morris, M. R., Lu, J. R., Matthews, K., Yelda, S., & Larkin, J. 2009, *ApJ*, 703, 1323  
 Dotti, M., Colpi, M., Haardt, F., & Mayer, L. 2007, *MNRAS*, 379, 956  
 Escala, A., Larson, R. B., Coppi, P. S., & Mardones, D. 2005, *ApJ*, 630, 152  
 Fakhouri, O., Ma, C.-P., & Boylan-Kolchin, M. 2010, *MNRAS*, 406, 2267  
 Ferrarese, L., van den Bosch, F. C., Ford, H. C., Jaffe, W., & O’Connell, R. W. 1994, *AJ*, 108, 1598  
 Ferrarese, L., et al. 2006a, *ApJL*, 644, L21  
 —. 2006b, *ApJS*, 164, 334  
 Figier, D. F., Rich, R. M., Kim, S. S., Morris, M., & Serabyn, E. 2004, *ApJ*, 601, 319  
 Freitag, M., Amaro-Seoane, P., & Kalogera, V. 2006, *ApJ*, 649, 91  
 Gaburov, E., Harfst, S., & Portegies Zwart, S. 2009, *New A*, 14, 630  
 Graham, A. W. 2004, *ApJL*, 613, L33  
 Graham, A. W., Erwin, P., Trujillo, I., & Asensio Ramos, A. 2003, *AJ*, 125, 2951  
 Graham, A. W., & Guzmán, R. 2003, *AJ*, 125, 2936  
 Graham, A. W., & Spitler, L. R. 2009, *MNRAS*, 397, 2148  
 Gualandris, A., & Portegies Zwart, S. 2007, *MNRAS*, 376, L29  
 Gualandris, A., Portegies Zwart, S., & Sipior, M. S. 2005, *MNRAS*, 363, 223  
 Gvaramadze, V. V., Gualandris, A., & Portegies Zwart, S. 2009, *MNRAS*, 396, 570  
 Harfst, S., Gualandris, A., Merritt, D., Spurzem, R., Portegies Zwart, S., & Berczik, P. 2007, *New Astronomy*, 12, 357  
 Hopman, C. 2009, *Classical and Quantum Gravity*, 26, 094028  
 Hopman, C., & Alexander, T. 2006, *ApJL*, 645, L133  
 Katz, N. 1991, *ApJ*, 368, 325  
 Kauffmann, G., & Haehnelt, M. 2000, *MNRAS*, 311, 576  
 Khan, F. M., Just, A., & Merritt, D. 2011, *ApJ*, 732, 89  
 King, I. 1962, *AJ*, 67, 471  
 Kocsis, B., & Tremaine, S. 2011, *MNRAS*, 412, 187  
 Kormendy, J. 1985, *ApJ*, 295, 73  
 Lauer, T. R., et al. 1995, *AJ*, 110, 2622  
 Löckmann, U., Baumgardt, H., & Kroupa, P. 2010, *MNRAS*, 402, 519  
 Makino, J., & Funato, Y. 2004, *ApJ*, 602, 93  
 Maness, H., et al. 2007, *ApJ*, 669, 1024  
 Martínez-Valpuesta, I., & Gerhard, O. 2011, *ApJL*, 734, L20+  
 Merritt, D. 2006, *ApJ*, 648, 976  
 —. 2009, *ApJ*, 694, 959  
 —. 2010, *ApJ*, 718, 739  
 —. 2012, *Dynamics and Evolution of Galactic Nuclei* (Princeton University Press)  
 Merritt, D., Alexander, T., Mikkola, S., & Will, C. M. 2010, *Phys. Rev. D*, 81, 062002  
 Merritt, D., & Cruz, F. 2001, *ApJL*, 551, L41  
 Merritt, D., Harfst, S., & Bertone, G. 2007a, *Phys. Rev. D*, 75, 043517  
 Merritt, D., Mikkola, S., & Szell, A. 2007b, *ApJ*, 671, 53  
 Merritt, D., & Poon, M. Y. 2004, *ApJ*, 606, 788  
 Merritt, D., & Szell, A. 2006, *ApJ*, 648, 890  
 Merritt, D., & Vasiliev, E. 2010, *ApJ*, 726, 61

- Mikkola, S., & Valtonen, M. J. 1992, *MNRAS*, 259, 115
- Milosavljević, M., & Merritt, D. 2001, *ApJ*, 563, 34
- Milosavljević, M., Merritt, D., Rest, A., & van den Bosch, F. C. 2002, *MNRAS*, 331, L51
- Oh, S., Kim, S. S., & Figer, D. F. 2009, *Journal of Korean Astronomical Society*, 42, 17
- O’Leary, R. M., & Loeb, A. 2008, *MNRAS*, 383, 86
- Perets, H. B., Gualandris, A., Kupi, G., Merritt, D., & Alexander, T. 2009, *ApJ*, 702, 884
- Peters, P. C. 1964, *Physical Review*, 136, 1224
- Preto, M., & Amaro-Seoane, P. 2010, *ApJL*, 708, L42
- Preto, M., Berentzen, I., Berczik, P., & Spurzem, R. 2011, *ApJL*, 732, L26+
- Preto, M., Merritt, D., & Spurzem, R. 2004, *ApJL*, 613, L109
- Quinlan, G. D. 1996, *New A*, 1, 35
- Rosenbluth, M. N., MacDonald, W. M., & Judd, D. L. 1957, *Physical Review*, 107, 1
- Schödel, R. 2011, in *Astronomical Society of the Pacific Conference Series*, Vol. 439, *Astronomical Society of the Pacific Conference Series*, ed. M. R. Morris, Q. D. Wang, & F. Yuan, 222–+
- Schödel, R., Merritt, D., & Eckart, A. 2009, *Astron. Astrophys.*, 502, 91
- Sesana, A., Gualandris, A., & Dotti, M. 2011, *MNRAS*, 415, L35
- Sesana, A., Haardt, F., & Madau, P. 2006, *ApJ*, 651, 392
- Seth, A., Agüeros, M., Lee, D., & Basu-Zych, A. 2008, *ApJ*, 678, 116
- Spitzer, L. 1987, *Dynamical evolution of globular clusters*, ed. Spitzer, L.
- Sridhar, S., & Touma, J. 1999, *MNRAS*, 303, 483
- Szell, A., Merritt, D., & Kevrekidis, I. G. 2005, *Physical Review Letters*, 95, 081102
- Terzić, B., & Graham, A. W. 2005, *MNRAS*, 362, 197
- Volonteri, M., Haardt, F., & Madau, P. 2003, *ApJ*, 582, 559
- Walcher, C. J., Böker, T., Charlot, S., Ho, L. C., Rix, H.-W., Rossa, J., Shields, J. C., & van der Marel, R. P. 2006, *ApJ*, 649, 692